# A Low-Complexity Bayesian Estimation Scheme for Speckle Suppression in Images

Rafat Rebhi Damseh

A Thesis

in

The Department

of

Electrical and Computer Engineering

Presented in Partial Fulfillment of the Requirements
for the Degree of Master of Applied Science at
Concordia University
Montreal, Quebec, Canada

April 2015

# CONCORDIA UNIVERSITY

## School of Graduate Studies

This is to certify that the thesis prepared

By: <u>Rafat Damseh</u>

Entitled: <u>A Low-Complexity Bayesian Estimation Scheme for Speckle</u> <u>Suppression in Images</u>

and submitted in partial fulfillment of the requirements for the degree of

M.A.Sc. Electrical & Computer Engineering

complies with the regulations of the University and meets the accepted standards with respect to originality and quality.

Signed by the final examining committee:

<u>Dr. M. Z. Kabir</u> Chair

<u>Dr. C. Wang</u> Examiner

<u>Dr. C. Y. Su</u> Examiner

<u>Dr. M. O. Ahmad</u> Supervisor

Approved by _____

Chair, Department of Electrical and Computer Engineering

_____

Dean, Faculty of Engineering and Computer Science

Date

# ABSTRACT

## A Low-Complexity Bayesian Estimation Scheme for Speckle Suppression in Images

Rafat Rebhi Damseh

Speckle noise reduction is a crucial pre-processing step for a successful interpretation of images corrupted by speckle noise, and thus, it has drawn a great deal of attention of researchers in the image processing community. The Bayesian estimation is a powerful signal estimation technique and has been widely used for speckle noise removal in images. In the Bayesian estimation based despeckling techniques, the choice of suitable signal and noise models and the development of a shrinkage function for estimation of the signal are the major concerns from the standpoint of the accuracy and computational complexity of the estimation.

In this thesis, a low-complexity wavelet-based Bayesian estimation technique for despeckling of images is developed. The main idea of the proposed technique is in establishing suitable statistical models for the wavelet coefficients of additively decomposed components, namely, the reflectance image and the signal-dependant noise, of the multiplicative degradation model of the noisy image and then in using these two statistical models to develop a shrinkage function with a low-complexity realization for the estimation of the wavelet coefficients of the noise-free image.

A study is undertaken to explore the effectiveness of using a two sided exponential distribution as a prior statistical model for the discrete wavelet transform (DWT) coefficients of the signal-dependant noise. This model, along with the Cauchy distribution, which is known to be a good model for the wavelet coefficients of the reflectance image, is used to develop a minimum mean square error (MMSE) Bayesian estimator for the DWT coefficients of the noise-free image. A low-cost realization of the shrinkage function resulting from the MMSE Bayesian estimation is proposed and its efficacy is verified from the standpoint of accuracy as well as computational cost.

The performance of the proposed despeckling scheme is evaluated on both synthetic and real SAR images in terms of the commonly used metrics, and the results are compared to that of some other state-of-the-art despeckling schemes available in the literature. The experimental results demonstrate the validity of the proposed despeckling scheme in providing a significant reduction in the speckle noise at a very low computational cost and simultaneously in preserving the image details.

# ACKNOWLEDGMENTS

"READ! IN THE NAME OF YOUR LORD WHO CREATED: 2 HE CREATED MAN
FROM A CLINGING FORM (LEECH-LIKE CLOT). 3 READ! YOUR LORD IS THE MOST
BOUNTIFUL ONE 4 WHO TAUGHT BY (MEANS OF) THE PEN, 5 WHO TAUGHT MAN WHAT
HE DID NOT KNOW."
[QUR'AN, 96:1-5]

All praise and thanks are due to Allah, the Almighty, who with His will I completed this work, and my utmost respect to his last prophet Mohammad (praise and peace be upon him), who delivered Allah's message of guidance to humanity.

I would like to express my deep gratitude to my supervisor Professor M. Omair Ahmed for his constant support, encouragement, patience, and invaluable guidance during this research. I am grateful to him for spending so many hours with me in discussion about this research and improving the writing of this thesis.

Sincere thanks go to my mother, father and family members for their encouragement and prayers during my research.

Special thanks from the bottom of my heart are to my wife, Lina, for her unconditional love, unlimited patience and constant support that made a successful completion of this work a reality. I would also like to mention my little son, Adam, whose charming and smiling face always vanishes all my hardships and provides me that extra strength to keep me going.

# CONTENTS

# LIST OF TABLES

# LIST OF FIGURES

# LIST OF ACRONYMS

CDF        Cumulative density function

DFT        Discrete Fourier transform

DWT        Discrete wavelet transform

ENL        Equivalent number of looks

FIR        Finite impulse response

GGD        Generalized Gaussian distribution

GL         Generalized Laplacian

MAP        Maximum a posteriori

ML         Maximum likelihood

MSE        Mean square error

MoLC       Method of log-cummulants

MoM        Method of moments

MMAE       Minimum mean absolute error

MMSE       Minimum mean square error

PR         Perfect reconstruction

PDF        Probability density function

SMG        Scale mixture of Gaussians

SNR        Signal to noise ratio

SSIM       Structural similarity

SNIG       Symmetric normal inverse Gaussian

SAR        Synthetic aperture radar

TSE        Two sided exponential

WT         Wavelet transform

# LIST OF SYMBOLS

| | |
|---|---|
| $\Re\{\cdot\}$ | Bayesian risk function |
| $\phi\{\cdot\}$ | Characteristic function |
| $\mathcal{C}$ | Correlation |
| $\text{Ci}\{\cdot\}$ | Cosine integral function |
| $C\{\cdot\}$ | Cost-of-error function |
| $\Sigma$ | Covariance matrix |
| $l$ | Decomposition level of DWT |
| $\delta\{\cdot\}$ | Delta function |
| $\mathcal{D}\{\cdot\}$ | Digamma function |
| $\gamma$ | Dispersion parameter of the Cauchy PDF |
| $\mathcal{L}$ | Dynamic range of pixel values |
| $\Upsilon$ | Euler-Mascheroni constant |
| $\text{E}_1\{\cdot\}$ | Exponential integral function |
| $\mathcal{F}$ | Forward transform of DFT |
| $\Gamma\{\cdot\}$ | Gamma function |
| $\mathcal{H}$ | Homogeneity |
| $\mathfrak{K}$ | Kortious |
| $h_\phi, h_\psi$ | Low- and high-pass filters of DWT |

| | |
|---|---|
| $E\{\cdot\}$ | Mathematical expectation |
| $\mu, \sigma^2$ | Mean and variance |
| $\mathcal{B}\{\cdot\}$ | Modified Second-kind Bessel function |
| $\mathcal{P}$ | Normalized co-occurrence |
| $\mathfrak{M}_n$ | n-th order moment |
| $\hat{k}_n$ | n-th order second-kind moment |
| $M$ | Number of looks of a SAR image |
| $N_v$ | Number of vanishing moments |
| $\mathcal{R}$ | Orientation of DWT coefficients |
| $X, \tilde{X}$ | Original and processed images |
| Re, Im | Real and imaginary parts of a complex number |
| $t_d$ | Root of the Hermite polynomial of order $d$ |
| $\beta$ | Scale parameter of the TSE PDF |
| $\phi, \psi$ | Scaling and wavelet functions of DWT |
| $\varphi\{\cdot\}$ | Second second-kind characteristic function |
| Si$\{\cdot\}$ | Sine integral function |
| $N_1 \times N_2$ | Size of a DWT subband |
| $\mathcal{M} \times \mathcal{N}$ | Size of an image |
| $K$ | Support size |
| $\vartheta_d$ | Weight of the Hermite polynomial of order $d$ |
| $c, s$ | Width and shape parameters in GL and SMG PDFs |

# CHAPTER 1

# Introduction

## 1.1 Introduction

Digital images contain a vital source of visual information, which is greatly affected due to the noise contamination of the images during their acquisition or transmission. Synthetic aperture radar (SAR) images are widely used in planetary exploration, such as in monitoring agricultural crops, conducting rescue operation and mapping of an earth surface. The use of SAR imaging systems is because of their capability in capturing images of a vast area of terrain irrespective of the weather or ambient illumination conditions. However, SAR imaging is subject to speckle noise contamination due to the coherent nature of the scattering phenomenon of electromagnetic waves involved in capturing SAR images [1]. Since the presence of speckle noise affects the task of human interpretation and scene analysis, removal or minimization of such a noise is a vital pre-processing step. Consequently, developing effective techniques for image despeckling has been a focus of many researchers in the image processing community.

In the early work for speckle noise removal, various spatial-domain algorithms have been developed [2-5]. However, these algorithms are limited in their capability in reducing the speckle noise significantly. In order to provide a better speckle noise

reduction, more promising techniques in the spatial domain, such as those using the improved sigma filter [6], nonlocal filtering [7], and the bilateral filtering [8], have been recently proposed. In general, the performances of these algorithms depend on the size of the filter window, and hence for a good performance, they consume large computational time.

Wavelet transform (WT) has been used to develop denoising algorithms [9-22] that operate in the frequency domain. Such algorithms have been proven to be effective in extracting signals from the noisy data due to following characteristics of WT:

- Excellent time-frequency / space-frequency characteristics
- Efficient modeling of the image wavelet coefficients using subband decomposition
- High energy-compaction property

Wavelet thresholding algorithm using a linear estimation scheme proposed by Donoho [9] is a revolutionary work for image denoising using wavelet transform. However, the main drawback of this thresholding algorithm is in the difficulty of determining a suitable threshold value. To circumvent this problem, a nonlinear estimator, which outperforms the linear estimators, has been developed by Simoncelli et al. [12] through the establishment of a wavelet shrinkage function based on Bayesian estimation formalism. The technique of Bayesian estimation in wavelet domain uses prior probability density functions (PDFs) to model the wavelet coefficients of the noisy and noise-free components of the observed image. This technique has been successfully applied for denoising images corrupted by the speckle noise based on different prior assumptions, such as alpha stable, generalized Gaussian, and Cauchy, for the wavelet coefficients [13-22].

## 1.2 Motivation

Bayesian based speckle noise minimization techniques in wavelet domain can be classified into two categories, namely, homomorphic [13-18] and non-homomorphic [19-22] schemes, depending on the way the multiplicative degradation model [23] of the observed image is transformed into an additive model. In general, the performances of the despeckling schemes in these two categories are greatly dependent on, first, the suitability of the PDFs used to model the wavelet coefficients, and second, the technique used for the realization of the Bayesian shrinkage function. The homomorphic scheme, in which the wavelet transform of the log-transformed noisy image is employed in order to obtain an additive degradation model, suffer from the drawbacks of the mean of the homogeneous areas in the observed image not being reserved and the signal variation being damped, due to the non-linear operation of the log-transformation. Also, this scheme is computationally more expensive due to the additional logarithmic and exponential operations. The non-homomorphic scheme, on the other hand, avoids these shortcomings by transforming the multiplicative degradation model into an additive one by decomposing it into noise-free and noise-dependant components. These two components are occasionally referred to as reflectance image and signal-dependant noise, respectively.

For the development of an efficient Bayesian despeckling scheme, which is based on the additive model of the observed signal, the choice of a suitable probability distribution to model the wavelet coefficients remains a major concern. The statistical model should employ a simple scheme for the estimation of its optimal parameters, which provide the best fit of the model to the empirical distribution of the wavelet coefficients.

Another concern while investigating a suitable statistical model is the complexity of the Bayesian estimation process. Consequently, one needs to pay special attention to the realization complexity of the Bayesian shrinkage function that results from employing the selected probabilistic model in one of the Bayesian frameworks, such as minimum mean square error (MMSE), minimum mean absolute error (MMAE) or maximum *a posteriori* (MAP) estimation of the wavelet coefficients.

## 1.3  Scope of the Thesis

The objective of this research work is to develop a non-homomorphic despeckling algorithm for images in a MMSE Bayesian framework. The main idea of the proposed despeckling scheme is in establishing suitable statistical models for the wavelet coefficients of the additively decomposed noise-free and signal-dependant noise components of the multiplicative degradation model of an image and then in using these statistical models to develop a shrinkage function with a low-complexity realization for the estimation of the wavelet coefficients of the noise-free image.

In this work, the two sided exponential (TSE) PDF is used as a prior distribution for the discrete wavelet transform (DWT) coefficients of the signal-dependant noise. This distribution, along with a Cauchy PDF used to model the reflectance component, is then employed to develop a MMSE Bayesian estimator for the DWT coefficients of the noise-free component of the observed image. A low-cost scheme for the realization of the shrinkage function resulting from an MMSE Bayesian estimation is proposed and its efficacy from the standpoint of accuracy as well as computational cost is studied. Experiments using synthetically-speckled and real SAR images are conducted to examine

4

the performance of the proposed wavelet-based Bayesian estimator in suppressing the speckle noise.

## 1.4 Organization of the Thesis

This thesis is organized as follows.

In Chapter 2, a brief overview of the necessary background material is presented in order to facilitate the development of the despeckling scheme proposed in this thesis. This overview consists of some preliminaries on wavelets and multi-resolution analysis of images, modeling of image wavelet coefficients and the theory of Bayesian estimation.

In Chapter 3, starting from the decomposition of the multiplicative model of an image contaminated by speckle noise into two additive components, namely, the signal-dependant noise and the reflectance image, the suitability of the two-sided exponential PDF to model the DWT coefficients of the former and that of the Cauchy PDF to model the to model the DWT coefficients of the latter are studied. Also, mechanisms for estimating the parameters of the PDFs employed to model the two additive components are provided. The formulation of the Bayesian shrinkage function resulting from the MMSE Bayesian framework is carried out to estimate the noise-free wavelet coefficients and a low-complexity scheme for its realization is devised.

In Chapter 4, experiments are performed to study the performance of the proposed despeckling scheme and those of other state-of-the-art despeckling schemes available in the literature when the schemes are applied to synthetically-speckled and real SAR images. The performances of the various schemes are compared using various objective indices such as signal-to-noise ratio (SNR), structural similarity (SSIM), homogeneity and

correlation. The various schemes are also compared in terms of the visual quality of the despeckled images and the execution time.

Finally, some concluding remarks highlighting the contribution of the thesis and scope of further research are provided in Chapter 5.

# CHAPTER 2

# A Brief Review of Background Material

Since the objective of this research work is to develop a Bayesian wavelet-based image despeckling scheme, some preliminaries of wavelets and Bayesian estimation are essential to conduct the research project undertaken in this thesis. In this chapter, an overview of wavelet theory and multi-resolution analysis is provided followed by a brief discussion on the commonly used PDFs for modeling the wavelet coefficients of an image. The formalism of Bayesian estimation, along with a brief overview of the cost functions used in this estimation, is also given.

## 2.1 Wavelets and Multi-resolution Analysis

The main idea behind the transformation of a digital signal is to be able to use some properties of the signal in the transformed domain that are not available in the original domain, e.g., time-domain or pixel-domain. One of the desirable features that should be obtainable by a transformation is its ability to provide a good sparse representation of the signal. The wavelet transform [24-28] offers this very important feature to the transformed signal. Wavelet transform is also considered to be a good transformation, since it provides

a signal representation that is localized at different decomposition levels (scales) leading to an easy detection and analysis of the local features of the signal [28].

Since in this thesis the signal modeling and the development of the proposed despeckling scheme are DWT based, in this section, an overview of the one-dimensional (1D) and two-dimensional (2D) DWTs is provided and the technique of obtaining the DWT coefficients using filter-banks [25-26] is discussed. Also, some of the wavelet functions used in DWT are presented and their suitability for various digital image processing applications is discussed.

## 2.1.1  1D and 2D DWTs

Let $v(i)$, $i = 1,2, \dots, \mathcal{M}$, represent a 1D signal of size $\mathcal{M}$. The DWT of the signal is given by

$$v(i) = \frac{1}{\sqrt{\mathcal{M}}} \left[ \sum_{p=1}^{\mathcal{M}} x_{\mathcal{J}}^{A}(p)\phi_{\mathcal{J}}^{A}(i,p) + \sum_{l=1}^{\mathcal{J}} \sum_{p=1}^{\mathcal{M}} x_{l}^{D}(p)\psi_{l}^{D}(i,p) \right] \qquad \textbf{(2.1)}$$

where $x_{\mathcal{J}}^{A}$ denotes the approximation coefficients in the highest decomposition level $\mathcal{J}$, $x_{l}^{D}$ denotes the detail coefficients in the decomposition level $l$ ($l = 1, 2, 3, \dots, \mathcal{J}$), $\phi_{\mathcal{J}}^{A}(i,p) = 2^{\frac{\mathcal{J}}{2}}\phi(2^{\mathcal{J}}i - p)$ and $\psi_{l}^{D}(i,p) = 2^{\frac{l}{2}}\psi(2^{l}i - p)$, $\phi$ and $\psi$ being, respectively, the scaling and wavelet functions. The approximation and detail coefficients can be obtained as

$$x_{\mathcal{J}}^{A}(p) = \frac{1}{\sqrt{\mathcal{M}}} \sum_{i=1}^{\mathcal{M}} v(i)\phi_{\mathcal{J}}^{A}(i,p) \qquad \textbf{(2.2)}$$

and

$$x_l^D(\wp) = \frac{1}{\sqrt{\mathcal{M}}} \sum_{i=1}^{\mathcal{M}} v(i)\psi_l^D(i,\wp) \qquad (2.3)$$

The scaling function $\phi$ and the wavelet function $\psi$ are chosen in such a way that the signal can be reconstructed from the DWT coefficients without any error. Since the DWT is based on a multi-resolution analysis, it is required that $\phi$ and $\psi$ satisfy the following two scale dilation equations:

$$\phi(i) = \sqrt{2} \sum_{u=-\infty}^{\infty} h_\phi(u)\, \phi(2i-u) \qquad (2.4)$$

$$\psi(i) = \sqrt{2} \sum_{u=-\infty}^{\infty} h_\psi(u)\, \phi(2i-u) \qquad (2.5)$$

where $h_\phi(u)$ and $h_\psi(u)$, respectively, are the scaling and wavelet vectors for the forward DWT. Using these relations, the DWT coefficients at $(l+1)$th decomposition level can be efficiently estimated from the knowledge of that at the adjacent $l$th level as [24]

$$x_{l+1}^A(\wp) = h_\phi(-u) * x_l^A(u)\big|_{u=2\wp,\wp\geq 0} \qquad (2.6)$$

$$x_{l+1}^D(\wp) = h_\psi(-u) * x_l^A(u)\big|_{u=2\wp,\wp\geq 0} \qquad (2.7)$$

where $*$ denotes the convolution operator. Thus, the approximation and detail coefficients at the decomposition level $(l+1)$ can be obtained by filtering the approximation coefficients at the decomposition level $l$ using $h_\phi(-u)$ and $h_\psi(-u)$, respectively, and then by down-sampling the filtered coefficients by 2. Similarly, the inverse transform relation of the DWT coefficients between the adjacent decomposition levels is given by [24]

$$x_l^A(\wp) = \hat{h}_\phi(u) * x_{l+1}^A(u)\big|_{u=\frac{\wp}{2},\ \wp\geq 0} + \hat{h}_\psi(u) * x_{l+1}^D(u)\big|_{u=\frac{\wp}{2},\ \wp\geq 0} \qquad (2.8)$$

where $\hat{h}_\phi(u)$ and $\hat{h}_\psi(u)$, respectively, are the scaling and wavelet vectors for the inverse DWT. From the above equation, it is noted that the approximation coefficients at the decomposition level $l$ can be obtained by filtering the approximate and detail coefficients at the decomposition level $(l + 1)$, up-sampled by 2, using $\hat{h}_\phi(u)$ and $\hat{h}_\psi(u)$, respectively, and adding the results.

In the theory of filter banks [25-26], $h_\phi(u)$ and $h_\psi(u)$ are often referred to as analysis filters, while $\hat{h}_\phi(u)$ and $\hat{h}_\psi(u)$ as synthesis filters. If a bank of analysis and synthesis filters exist, such that the input signal to the filter bank is identical to output signal from the filter bank, except for a possible delay or overall scaling factor, then the analysis and synthesis filters of the bank are said to be a perfect reconstruction (PR) pair [26]. By implementing a PR pair of analysis and synthesis filters, one can simply obtain the forward and inverse DWT without computing the wavelet functions. A simple block diagram of the forward and inverse 1D DWT using the analysis and synthesis filters between two adjacent decomposition levels is shown in Figure 2.1. We note from this figure that there is no data redundancy in the DWT coefficients due to the down sampling.

**(a)**



**(b)**
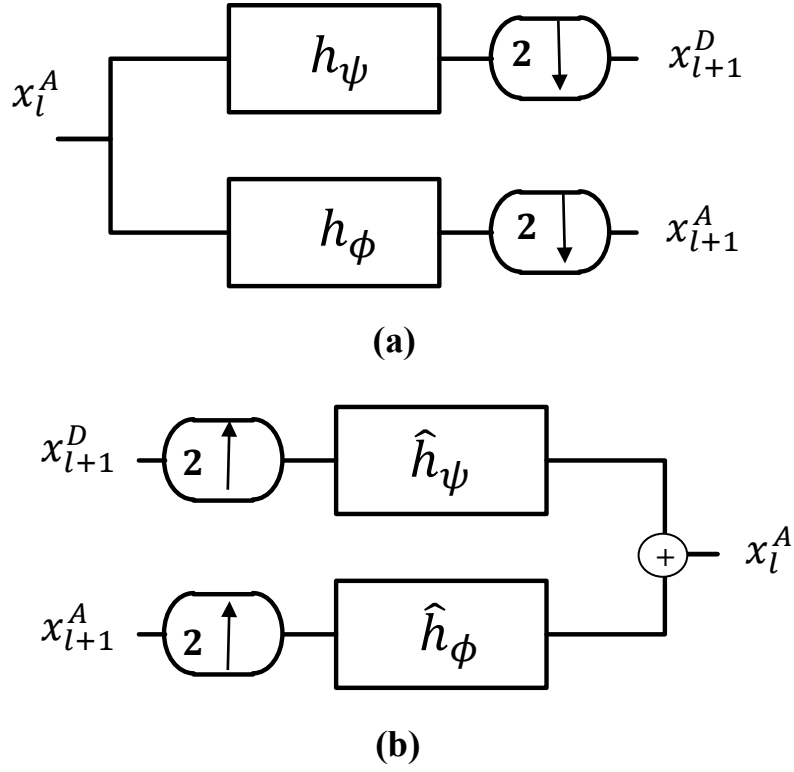
Figure 2.1: Block diagram of the 1D DWT using analysis and synthesis filters. (a) Forward transform. (b) Inverse transform.

To obtain the 2D DWT, we let $v(i,j)$, $i = 1, 2, \dots, \mathcal{M}$, $j = 1, 2, \dots, \mathcal{N}$, represent a 2D signal. The DWT of this signal is given by [28]

$$
v(i,j) = \frac{1}{\sqrt{MN}}
\left[
\begin{array}{l}
\displaystyle\sum_{p=1}^{\mathcal{M}}\sum_{q=1}^{\mathcal{N}} x_{\mathcal{J}}^A(p,q)\, \Phi_{\mathcal{J}}^A(i,j,p,q) + \\[2ex]
\displaystyle\sum_{l=1}^{\mathcal{J}}\sum_{\mathcal{R}\in\mathfrak{h},\mathfrak{v},\mathfrak{d}}\sum_{p=1}^{\mathcal{M}}\sum_{q=1}^{\mathcal{N}} x_l^{\mathcal{R}}(p,q)\, \Psi_l^{\mathcal{R}}(i,j,p,q)
\end{array}
\right]
\tag{2.9}
$$

where $x_l^{\mathcal{R}}(\mathcal{R}\in\mathfrak{h},\mathfrak{v},\mathfrak{d})$ is the detail coefficients in the decomoposition level $l$ ($l = 1, 2, 3, \dots, \mathcal{J}$) of orientation $\mathcal{R}$, and $\Phi$ and $\Psi$, respectively, denote the 2D scaling and

11

wavelet functions. By using separable scaling and wavelet functions, the 2D scaling and wavelet functions can be represented in terms of 1D scaling and wavelet functions as

$$\Phi_J^A(i,j,p,q) = 2^{J/2}\,\phi(2^J i - p)\,\phi(2^J j - q) \qquad \textbf{(2.10a)}$$

$$\Psi_l^{\mathfrak{h}}(i,j,p,q) = 2^{l/2}\,\phi(2^l i - p)\,\psi(2^l j - q) \qquad \textbf{(2.10b)}$$

$$\Psi_l^{\mathfrak{v}}(i,j,p,q) = 2^{l/2}\,\psi(2^l i - p)\,\phi(2^l j - q) \qquad \textbf{(2.10c)}$$

$$\Psi_l^{\mathfrak{d}}(i,j,p,q) = 2^{l/2}\,\psi(2^l i - p)\,\psi(2^l j - q) \qquad \textbf{(2.10d)}$$

The approximate and detail coefficients of the 2D DWT are obtained using the following two equations:

$$x_J^A(p,q) = \frac{1}{\sqrt{\mathcal{MN}}}\sum_{i=1}^{\mathcal{M}}\sum_{j=1}^{\mathcal{N}} v(i,j)\,\Phi_J^A(i,j,p,q) \qquad \textbf{(2.11)}$$

$$x_l^{\mathcal{R}}(p,q) = \frac{1}{\sqrt{\mathcal{MN}}}\sum_{i=1}^{\mathcal{M}}\sum_{j=1}^{\mathcal{N}} v(i,j)\,\Psi_l^{\mathcal{R}}(i,j,p,q) \qquad \textbf{(2.12)}$$

From these relations, it is noted that the DWT coefficients are clustered into subbands of different decomposition levels and orientations. The subbands HL, LH and HH at the $l$th decomposition level contain the detail coefficients of the horizontal, vertical, and diagonal orientations, viz., $x_l^{\mathfrak{h}}$, $x_l^{\mathfrak{v}}$ and $x_l^{\mathfrak{d}}$, respectively. The subband LL at level $J$, contains the approximation coefficients that are the low-pass-filtered version of the original signal. This means that at each subsequent decomposition level $(l + 1)$, the subband LL at the $l$th level is further decomposed again into four subbands, namely, LL, HL, LH and HH, at the $(l + 1)$th level. Figure 2.2 shows the subband representation of a 3-level 2D DWT. It is noted that the use of the separable functions given by (2.10) in (2.11) and (2.12) converts the operation of the 2D DWT into that of two 1D DWTs.
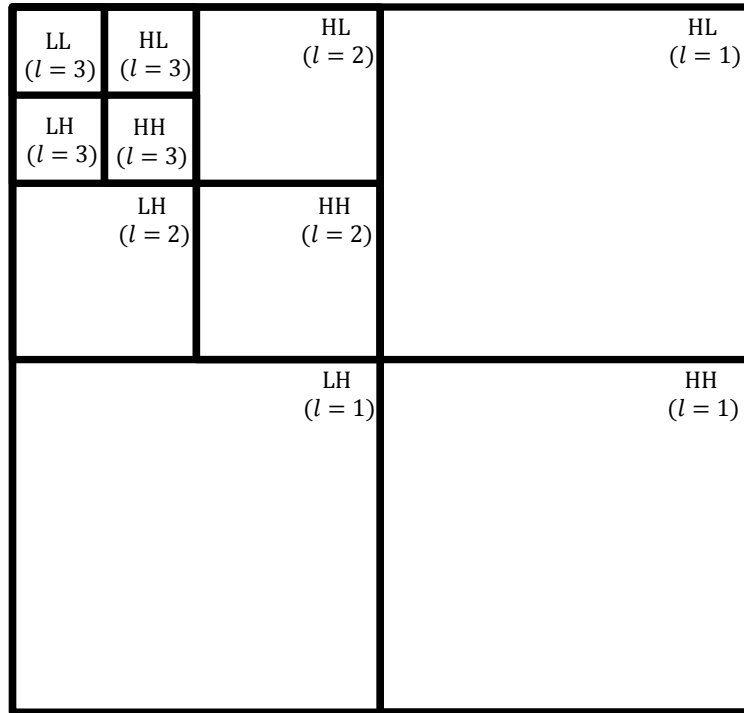
Figure 2.2: Subband representation of a 3-level 2D DWT.

Now, similar to the technique used in the case of the 1D DWT, an efficient implementation of forward and inverse 2D DWT can be obtained by using a bank of analysis and synthesis filters. Block diagram of the forward and inverse 2D DWT is shown in Figure 2.3. It is noted from this figure that both the forward and inverse transforms use a two-stage filtering operation, one through the columns of a 2D array and the other through the rows of a 2D array. A filer bank can be designed to be orthogonal or biorthogonal. An orthogonal filter bank has the coefficients of its analysis filters being time reversal of that of its synthesis filters. However, for a biorthogonal filter bank, the coefficients of the analysis filters do not have to be time reversal of that of the synthesis filters, and thus brings

13
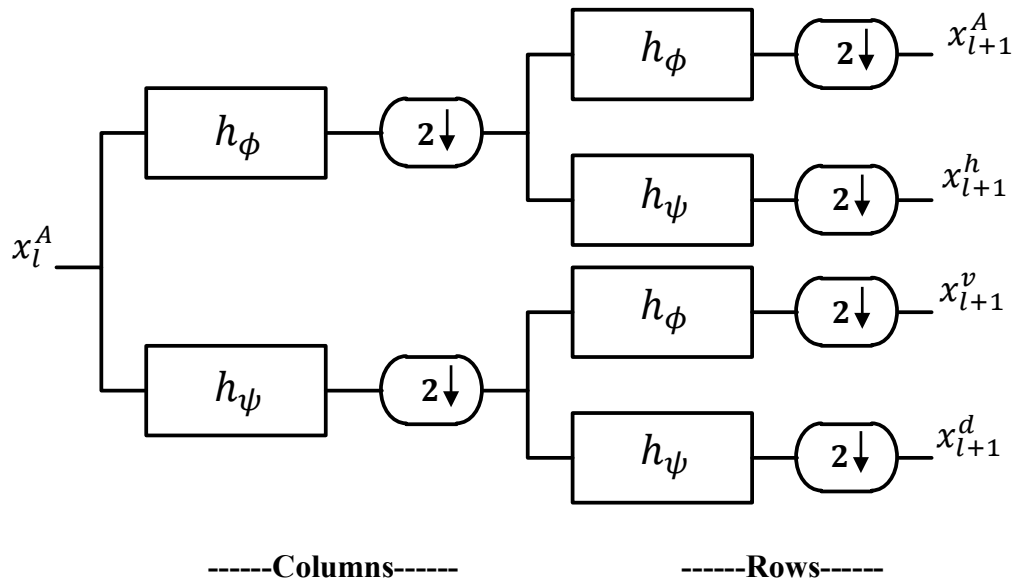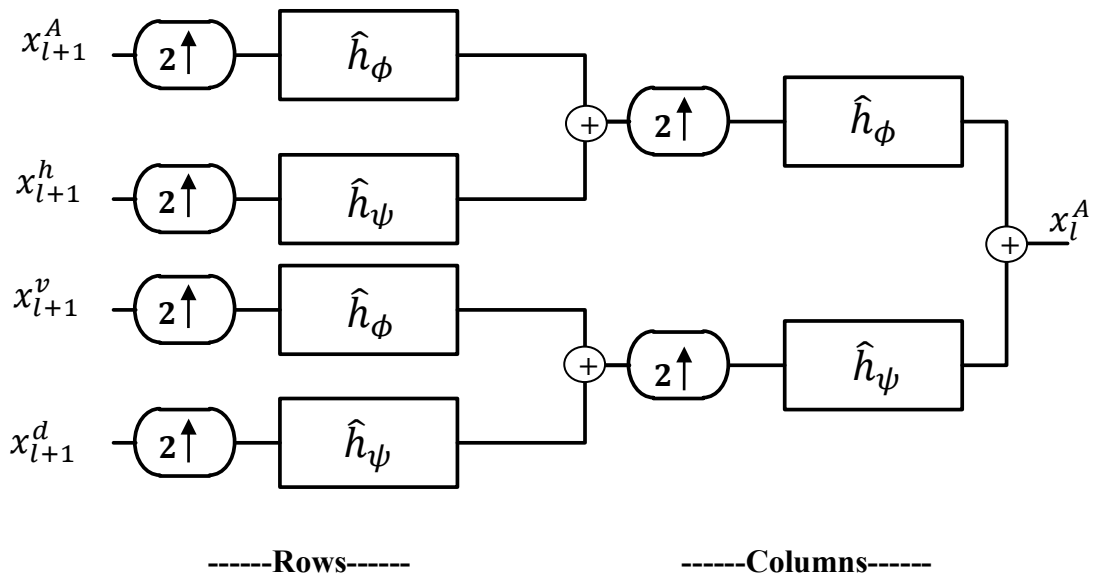
Figure 2.3: Block diagram of the 2D DWT using synthesis and analysis filters. (a) Forward 2D DWT using analysis filters. (b) Inverse 2D DWT using synthesis filters.

more freedom to the design of the filters. For both the orthogonal and biorthogonal filter banks, PR imposes the condition that its analysis and synthesis filters satisfy the following two relations [29]:

$$\mathcal{F}h_\phi\big(-(w+\pi)\big)\,\mathcal{F}\hat{h}_\phi(w) + \mathcal{F}h_\psi(-(w+\pi))\,\mathcal{F}\hat{h}_\psi(w) = 0 \qquad \textbf{(2.13)}$$

$$\mathcal{F}h_\phi(-w)\,\mathcal{F}\hat{h}_\phi(w) + \mathcal{F}h_\psi(-w)\,\mathcal{F}\hat{h}_\psi(w) = 2 \qquad \textbf{(2.14)}$$

where $\mathcal{F}h_\phi$, $\mathcal{F}\hat{h}_\phi$, $\mathcal{F}h_\psi$ and $\mathcal{F}\hat{h}_\psi$ are the Fourier transforms of $h_\phi$, $\hat{h}_\phi$, $h_\psi$ and $\hat{h}_\psi$, respectively.

## 2.1.2 Choosing a Wavelet

A DWT with desired features is obtained by constructing suitable scaling and wavelet functions. As previously seen, DWT is performed by using a bank of analysis and synthesis filters. Thus, it is with an appropriate design of these filters, one should be able to realize scaling and wavelet functions with the desired features. Often a DWT must provide a signal representation with as few non-negligible coefficients as possible. Apart from the nature of the signal to be decomposed into wavelet coefficients, the number of such coefficients depends on the number of vanishing moments of the wavelet function $\psi$ [25] and the size of its support. There are two other properties of $\psi$, regularity and symmetry, that help in providing a DWT with certain characteristics.

The function $\psi(t)$, $t$ being a real variable, can be a wavelet function if it oscillates, averaging to zero, i.e., $\int_{-\infty}^{\infty} \psi(t)dt = 0$, and is well localized, i.e., rapidly decreases to zero as $|t|$ increases [28]. The influence of the properties of a wavelet function on the DWT characteristics is described below.

**Number of vanishing moments:** A wavelet function satisfying the following equation

$$\int_{-\infty}^{\infty} t^r \psi(t) dt = 0, \qquad 0 < r \leq N_v - 1 \tag{2.15}$$

is said to have $N_v$ vanishing moments. One should construct a $\psi$ giving the number of vanishing moments $N_v$ to be as large as possible in order to produce a large number of small DWT coefficients.

**Support size:** The construction of a wavelet function with a small support size also reduces the number of non-negligible DWT coefficients. A wavelet function with a compact support $K$ is realized through designing finite impulse response (FIR) analysis and synthesis filters, which are inherently stable.

**Regularity:** The regularity of a wavelet function gives an approximate measure of the number of continuous derivatives that the function possesses. The regularity, therefore, gives a measure of the smoothness of the wavelet function, with higher regularity implying a smoother wavelet. The regularity of a wavelet function has a cosmetic influence on the error introduced from thresholding or quantizing the DWT coefficients. When reconstructing a signal from its thresholded or quantized wavelet coefficients, an error is introduced in the reconstructed signal. If $\psi(t)$ is smooth then this error is also smooth [30].

**Symmetry:** A symmetric wavelet function $\psi(t)$ gives equal weighting about the midpoint $t_0$ of its support. A DWT with symmetric wavelet functions permits a symmetric boundary extension of the transformed signal that minimizes the border artifacts [31-32]. Symmetric wavelet functions are realized when the analysis and synthesis filters have linear phase responses.

With an orthogonal bank of analysis and synthesis filters, it is difficult to realize a wavelet function that has simultaneously a large number of vanishing moments $N_v$ and a

16

small support size $K$, since a reduction in $K$ also decreases $N_v$. The best compromise between $K$ and $N_v$ is achieved by the Daubechies wavelets, denoted by $dbN_v$ [33]. For Daubechies wavelets, the relation between $K$ and $N_v$ is given by $K = 2N_v - 1$. This relationship is the best compromise in that it gives a smaller support size $K$ than that given by other orthogonal wavelets for a given value of $N_v$. Hence, for a given $N_v$, Daubechies wavelets provide a more compact support size than that provided by other orthogonal wavelets. The shortest member of the Daubechies wavelets, *db1*, is the Haar wavelet. Except for the Haar wavelet, orthogonal wavelets with compact support, including Daubechies wavelets, cannot be symmetrical [26]. The least asymmetrical ones, also constructed by Daubechies, are the *symlet* wavelets denoted as *symN_v* (the relation $K = 2N_v - 1$ still applies to *symlet* wavelets).

The objective of realizing wavelet functions with a small support size and a large number of vanishing moments is more easily achievable when using biorthogonal filter banks [34]. For biorthogonal wavelets, in contrast to orthogonal wavelets, the properties of compact support and symmetry are achieved simultaneously. The choice of a wavelet, whether orthogonal or biorthogonal, depends on its application. For image compression applications, biorthogonal wavelets can improve the compression performance, since it permits a symmetrical boundary extension of the transformed coefficients. On the other hand, image denoising applications require high de-correlation of the transformed coefficients, which is easier to achieve in the case of orthogonal wavelets.

## 2.2 Existing PDFs for Modeling of DWT Coefficients

Statistical modeling of the DWT coefficients is an important issue in many disciplines such digital image processing. The performance of a DWT-based speckle suppression technique is greatly influenced by the suitability of a statistical model of the image DWT coefficients. The statistical models of DWT coefficients can be divided into two categories: nonparametric [35-36] and parametric [13-22]. In a nonparametric model, no probability distribution function is assumed, meaning that the desired distribution is totally data-driven. Since nonparametric modeling involves complex computation [35], it is in general time-consuming and cannot be adopted in many applications. Alternatively, the parametric modeling has been used, especially when the distribution of a data has a known shape. Parametric modeling essentially boils down to finding the parameter values of a chosen PDF that can best match the empirical distribution of the data.

A common assumption in a parametric modeling of the DWT coefficients is that the PDFs of these coefficients are independent and identically distributed. Let $x(p,q)$ represent the wavelet coefficient at the index $(p,q)$ of a subband of the 2D DWT and $p_X(x)$ be the PDF of the random variable $x$. A brief overview of some of the PDFs used for modeling the DWT coefficients is presented next.

### 2.2.1 Generalized Laplacian (GL) PDF

The histograms of the DWT coefficients are typically sharply peaked at zero. Hence, the zero-mean GL PDF defined as

$$p_X(x) = \frac{1}{\frac{2c}{s}\Gamma\left(\frac{1}{s}\right)}e^{-\left|\frac{x}{c}\right|^2} \tag{2.16}$$

18

where $c$ $(c > 0)$ is the width parameter, $s$ $(1 < s < 2)$ is the shape parameter and $\Gamma(w) = \int_0^\infty t^{w-1} e^{-t} dt$ is the Gamma function, has been commonly used to model the DWT coefficients [24]. It is to be noted that (2.16) reduces to a Laplacian PDF when $s = 1$ and to a Gaussian PDF when $s = 2$. Therefore, some researchers have also referred to the above model as the generalized Gaussian distribution (GGD). The model parameters $s$ and $c$ can be calculated from the samples of the DWT coefficients. Specifically, if $\sigma_x^2$ is the sample variance and $\mathfrak{K}_x$ is the kurtosis of the data samples of the DWT coefficients, then the following formulas are used to estimate $s$ and $c$:

$$\sigma_x^2 = \frac{c^2 \Gamma\left(\frac{3}{s}\right)}{\Gamma\left(\frac{1}{s}\right)} , \qquad \mathfrak{K}_x = \frac{\Gamma\left(\frac{1}{s}\right)\Gamma\left(\frac{5}{s}\right)}{\Gamma^2\left(\frac{3}{s}\right)} \tag{2.17}$$

## 2.2.2 Scale Mixture of Gaussian (SMG) PDFs

By using a scale mixture model, a variety of other models can be derived. In the SMG PDF, the random variable $\boldsymbol{x}$ is assumed to be a product of a Gaussian random vector $\boldsymbol{X}$, whose density is determined by the covariance matrix $\Sigma_X$ , and an independent hidden positive scalar random variable $\sqrt{t}$ (usually known as the multiplier); this PDF is given as [37]

$$p_{\boldsymbol{X}}(\boldsymbol{x}) = \frac{1}{\sqrt{(2\pi)^N |t\Sigma_X|}} \int e^{\left[-\frac{\boldsymbol{x}^T (t\Sigma_X)^{-1}\boldsymbol{x}}{2}\right]} p_t(t)\, dt \tag{2.18}$$

where $N$ is the number of DWT coefficients $\boldsymbol{x}$ of a subband. The most critical part in evaluating the SMG PDF is the estimation of the density function for $t$. In general, $p_t(t)$ can be approximated as log-normal PDF [38] given by

$$p_t(t) = \frac{1}{t\sqrt{2\pi\sigma_L^2}} \, e^{\left[-\frac{(\log t - \mu_L)^2}{2\sigma_L^2}\right]} \tag{2.19}$$

where $\mu_L = -\log(\sigma_t^2 + 1)/2$ and $\sigma_L^2 = \log(\sigma_t^2 + 1)$, $\sigma_t^2$ being the variance of the random variable $t$. The variance $\sigma_t^2$ can be calculated from of the second- and fourth-order moments of the data samples of the DWT coefficients as $\sigma_t^2 = \mathfrak{M}_{4x}/3\sigma_x^2$, where $\mathfrak{M}_{4x}$ is the fourth-order moment.

### 2.2.3 Symmetric Normal Inverse Gaussian (SNIG) PDF

The SNIG PDF is a mixture of the inverse Gaussian and standard Gaussian PDFs , and is given by

$$p_X(x) = \mathcal{A} \frac{\mathcal{B}_1(\hat{s}\sqrt{\hat{c}^2 + x^2})}{\sqrt{\hat{c}^2 + x^2}} \tag{2.20}$$

where $\hat{s}$ ($\hat{s} > 0$) is the shape parameter, $\hat{c}$ ($\hat{c} > 0$) is the scale parameter, $\mathcal{A} = \frac{\hat{c}\hat{s}\,e^{\hat{c}\hat{s}}}{\pi}$ and $\mathcal{B}_1$ is the modified second-kind Bessel function [39] of the first order. The parameters $\hat{s}$ and $\hat{c}$ are estimated using the sample variance and Kurtosis given by

$$\sigma_x^2 = \frac{\hat{c}}{\hat{s}}, \qquad \mathfrak{K}_x = \frac{3(1 + \hat{s}\hat{c})}{\hat{s}^2} \tag{2.21}$$

The SNIG PDF has been used to model the DWT coefficients of log-transformed images that are common in SAR and medical applications [40], [41].

## 2.3 Bayesian Estimation

Bayesian Estimation is used to develop a statistical scheme to estimate noise-free signals from their noisy observations [42], e.g., image signals contaminated by speckle noise. To estimate the noise-free signal from its noisy observation using Bayesian

estimation, the prior knowledge of the distribution of the noise-free signal samples is combined with the information contained in the observed signal samples. Bayesian estimation is based essentially on minimizing the Bayesian risk function. Let $x$ denotes an unknown noise-free signal and $y$ its noisy observation. The Bayesian estimation $\hat{x}$ of $x$ is based on minimizing the Bayesian risk function defined as an average of the cost-of-error function $C(x, \hat{x})$:

$$\Re(\hat{x}) = E\{C(x, \hat{x})\} = \int_x \int_y C(x, \hat{x}) \, p_{X,Y}(x, y) \, dx \, dy \qquad (2.22)$$

where $E\{C(x, \hat{x})\}$ is the expectation value of the cost-of-error function $C(x, \hat{x})$ and $p_{X,Y}(x, y)$ is the joint probability density function of $x$ and $y$. Since $p_{X,Y}(x, y) = p_Y(y) \, p_{X|Y}(x|y)$, the Bayesian risk function can be re-written as

$$\Re(\hat{x}) = \int_x \int_y C(x, \hat{x}) \, p_{X|Y}(x|y) p_Y(y) \, dx dy \qquad (2.23)$$

For a given observation $y$, The PDF $p_Y(y)$ is constant and has no effect on the minimization of the Bayesian risk function. Hence, without a loss of generality, the Bayesian risk function given by (2.23) can be re-written as a conditional risk function:

$$\Re(\hat{x}|y) = \int_x C(x, \hat{x}) \, p_{X|Y}(x|y) \, dx \qquad (2.24)$$

The Bayesian estimates obtained from the minimization of the conditional Bayesian risk (2.24) function is given by

$$\hat{x}_{Bayesian} = \arg \min_{\hat{x}} \, \mathcal{R}(\hat{x}|y) = \arg \min_{\hat{x}} \int_x C(x, \hat{x}) \, p_{X|Y}(x|y) \, dx \qquad (2.25)$$

Next, we present a brief overview of two Bayesian estimation schemes, MAP and MMSE. Each scheme uses a cost-of-error function that is different from the one used by the other.

### 2.3.1 MAP Estimation

The Bayesian MAP estimation framework uses a uniform cost-of-error function defined as

$$C(x, \hat{x}) = 1 - \delta(x, \hat{x}) \tag{2.26}$$

where $\delta(x, \hat{x})$ is the delta function. The substitution of this cost-of-error function in the formula of the Bayesian risk function yields

$$\mathfrak{R}_{MAP}(\hat{x}|y) = \int_{x} [1 - \delta(x, \hat{x})]\, p_{x|y}(x|y)\, dx = 1 - p_{x|y}(\hat{x}|y) \tag{2.27}$$

In (2.27), the MAP estimates $\hat{x}_{\text{MAP}}$ are obtained from a minimisation of the risk function or equivalently a maximization of the posterior function $p_{\hat{x}|y}(x|y)$. Hence, the MAP estimates $\hat{x}_{\text{MAP}}$ can be obtained as

$$\hat{x}_{MAP} = \arg\max_{x} \ p_{x|y}(x|y) = \arg\max_{x} \ p_{y|x}(y|x)\, p_{x}(x) \tag{2.28}$$

### 2.3.2 MMSE Estimation

In the Bayesian MMSE estimation, we have $C(x, \hat{x}) = (\hat{x} - x)^2$, and thus, the Bayesian risk function is given by

$$\mathfrak{R}_{MMSE}(\hat{x}|y) = \int_{x} (\hat{x} - x)^2\, p_{x|y}(x|y)\, dx \tag{2.29}$$

The cost-of-error function used in (2.29) is commonly referred to as the quadratic cost function and the use of this function can accentuate the effects of large errors. Assuming that the quadratic cost function is differentiable and has a well-defined minimum, the MMSE estimates can be obtained by setting the gradient of the conditional Bayesian risk function to zero. The gradient of the conditional Bayesian risk function is computed as

22

$$\frac{\partial \mathfrak{R}_{MMSE}(\hat{x}|y)}{\partial \hat{x}} = 2\hat{x} \int_x p_{x|y}(x|y)\, dx - 2 \int_x x\, p_{x|y}(x|y)\, dx \qquad \textbf{(2.30)}$$

Since the first integral on the right side of (2.30) is equal to one, we have

$$\frac{\partial \mathfrak{R}_{MMSE}(\hat{x}|y)}{\partial \hat{x}} = 2\hat{x} - 2 \int_x x\, p_{x|y}(x|y)\, dx \qquad \textbf{(2.31)}$$

By setting (3.31) to zero, the MMSE estimates can be obtained as

$$\hat{x}_{MMSE} = \int_x x\, p_{x|y}(x|y)\, dx \qquad \textbf{(2.32)}$$

## 2.4 Summary

In this chapter, some preliminaries on the 1D and 2D DWTs have been presented along with the technique of using the concept of filter banks to obtain these transforms. A brief overview of some of the wavelets, along with the type of filter banks used for their realization, has also been given. Some of the existing PDFs used for the modeling of the wavelet coefficients have been briefly discussed. Finally, a brief discussion on the theory of Bayesian estimation and some of the Bayesian estimation schemes has been presented.

# CHAPTER 3

# Non-Homomorphic Bayesian Scheme for Speckle Suppression in Images

## 3.1 Introduction

In images corrupted by speckle noise, such as in SAR images, the interpretation and analysis of the image content is a difficult task. Hence, speckle noise reduction is a critical step in the processing of these images. The wavelet-based Bayesian estimation is a powerful denoising technique and has been widely used for speckle noise removal in images. As explained in Chapter 1, in developing of an efficient wavelet-based Bayesian despeckling scheme, the choice of a suitable probability distribution to model the wavelet coefficients and achieving a low-complexity realization of the Bayesian shrinkage function are two major concerns. In this chapter, by addressing these concerns, a new wavelet-based Bayesian estimation technique for despeckling of images is proposed. The main idea of the proposed technique is in establishing suitable statistical models for the wavelet coefficients of additively decomposed components, i.e., the reflectance image and the signal-dependant noise, of the multiplicative degradation model of a speckled image, and then in using these two statistical models to develop a shrinkage function with a low-complexity realization to estimate the noise-free wavelet coefficients. The effectiveness of using a two sided

24

exponential PDF as a prior distribution for the DWT coefficients of the signal-dependant noise is explored. This distribution modeling the wavelet coefficients of the noisy component, along with a Cauchy distribution modeling the wavelet coefficients of the reflectance image, is employed to formulate an MMSE Bayesian shrinkage function to obtain the estimates of the noise-free wavelet coefficients. A low-cost scheme for the realization of the resulting shrinkage function is proposed.

## 3.2 Modeling of Wavelet Coefficients

The multiplicative degradation model of a speckle-corrupted image $g(i,j)$ in the spatial domain is given by

$$g(i,j) = v(i,j)s(i,j) \tag{3.1}$$

where $v(i,j)$ and $s(i,j)$ denote the noise-free image and the speckle noise, respectively. This model of the noisy observation of $v(i,j)$ can be additively decomposed as a noise-free signal component and a signal-dependant noise:

$$g(i,j) = v(i,j) + (s(i,j) - 1)v(i,j)$$

$$= v(i,j) + u(i,j) \tag{3.2}$$

where $u(i,j) = (s(i,j) - 1)v(i,j)$ represents the signal-dependant noise. Taking the discrete wavelet transform of (3.2) at level $l$, we have

$$y^{[l,k]}(p,q) = x^{[l,k]}(p,q) + n^{[l,k]}(p,q) \tag{3.3}$$

where $y^{[l,k]}(p,q)$, $x^{[l,k]}(p,q)$ and $n^{[l,k]}(p,q)$ denote, respectively, the $(p,q)$th wavelet coefficient of the observed image, the corresponding noise free image and the corresponding additive signal-dependant noise at $k = 1, 2, 3$ and $4$. The values of $k$ denote the four subbands, LL, LH, HL and HH, respectively. In order to simplify the

25

notation, we will henceforth drop both the superscripts $l$ and $k$ and the index $(p, q)$ in this work.

### 3.2.1 Modeling of the Signal-dependant Noise

This subsection is intended to provide a prior model of the DWT coefficients of the signal-dependant noise $n$. In order to study the characteristics of the distribution of $n$, the speckle noise $s$ is synthetically-generated, and then, $u$ is computed as $(s-1)v$, where $v$ is a noise-free test image. The speckle noise $s$ for the intensity format of an $M$-look SAR image can be synthetically generated by using the PDF of a unit-mean, $1/M$-variance Gamma random variable, i.e., $p_S(s) = M^M s^{(M-1)} e^{-(Ms)}/\Gamma(M)$, where $s$ is the speckle noise random variable. The empirical distributions of $n$ for the LH, HL and HH subband coefficients of the *Lena*, *Boat* and *Pirate* images for $M$=32 are depicted in Figure 3.1 It is seen from this figure that the DWT coefficients $n$ tend to have a unimodal symmetric heavy-tailed statistical distribution. Also, it is obvious that the tail part of the empirical distribution of $n$ decays at a low rate. Hence, we propose to use a two-sided exponential (TSE) PDF given by

$$p_n(n) = \frac{1}{2\beta} \exp\left\{-\frac{|n|}{\beta}\right\} \tag{3.4}$$

where $\beta$ is a positive real constant referred to as the scale parameter, to model $n$. The underlying reasons for the choice of the TSE PDF are as follows. First, the tail part of the empirical distribution resembles that of the TSE PDF well. Second, since this PDF has only one parameter, an estimation of this parameter should be relatively less complex. We now examine the suitability of the TSE PDF in comparison to that of the zero-mean Gaussian
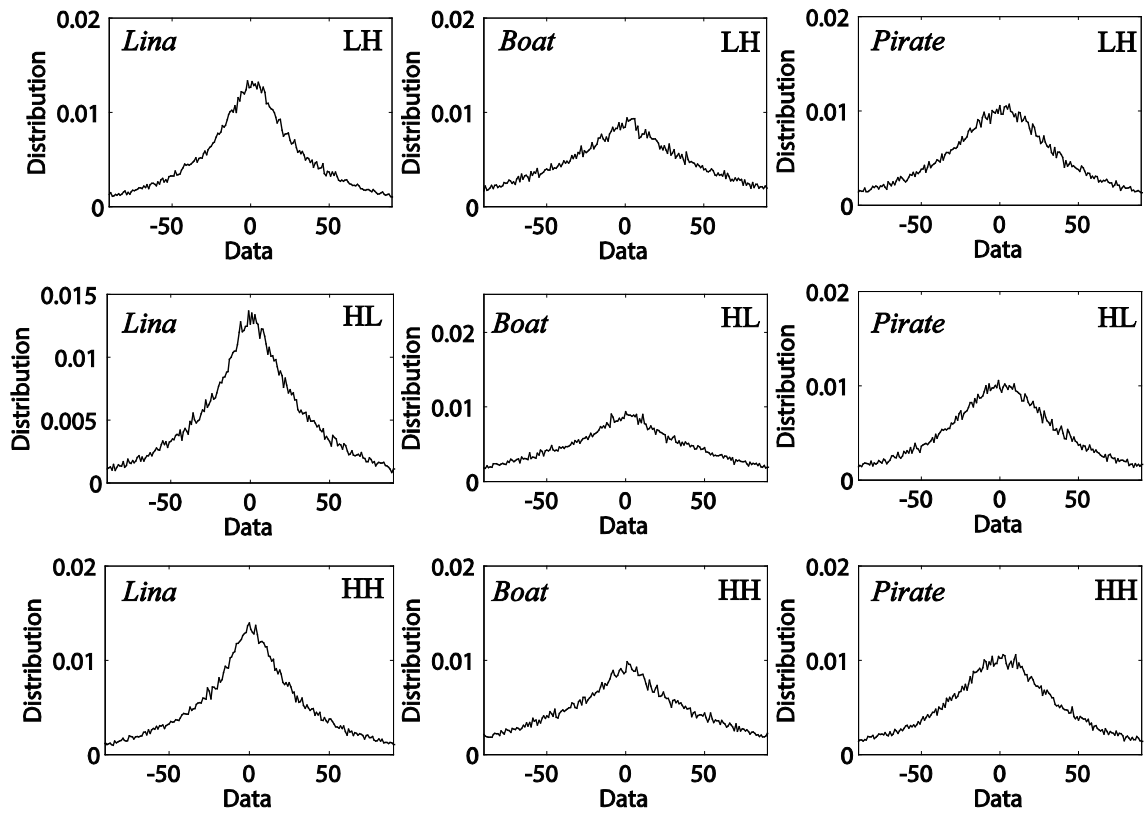
Figure 3.1: Empirical distributions of the DWT coefficients ($l$=1) of the signal-dependant noise $n$ for various images.

or SNIG PDFs in modeling the DWT coefficients of the signal dependant noise of SAR images. The latter two PDFs have been commonly used in the literature to model $n$ [19-21]. The zero-mean Gaussian PDF has only one parameter whereas SNIG PDF has two, namely, the shape and width parameters. The Kolmogorov-Smirnov distance, defined by

$$D_{KS} = \max_n \left| P_{emp}(n) - P(n) \right| \tag{3.5}$$

where $P_{emp}(n)$ and $P(n)$, respectively, represent the empirical and theoretical cumulative density functions (CDF), is used as a metric to quantify the modeling performance. Table 3.1 shows the values of $D_{KS}$ when the Gaussian, SNIG and TSE PDFs are used to model the HL, LH and HH subbands of the *Lena, Boat,* and *Pirate* images at $l = 1$ and 2. The values of the $D_{KS}$ metric in this table are obtained for two different values of *M,* 4 and 32. It should be noted that the lower the value of *M*, the higher is the level of the speckle. It is seen from this table that, in all cases, the Gaussian distribution is not a suitable choice to model $n$. It is also seen that the $D_{KS}$ values for TSE and SNIG models are quite close. In general, the $D_{KS}$ values of TSE PDF are slightly lower than that of SNIG PDF. Figures 3.2, 3.3 and 3.4 depict the modeling performances of the Gaussian, SNIG and TSE PDFs by providing the plots of their distributions along with the empirical distributions of the HL, LH and HH subbands of the *Lena, Boat* and *Pirate* images at $l = 1$ and $M = 32$. The figures also include a magnified view of the tail end of each of the distributions. It is seen from these figures that, in comparison to the Gaussian PDF, SNIG and TSE PDFs provide better fits with the empirical distribution with the TSE PDF showing a closer fit in the tail parts of the distributions. Thus, in view of this study, which shows that TSE PDF,

Table 3.1: Values of the Kolmogorov-Smirnov distance for HL, LH and HH subbands of the *Lena*, *Boat* and *Pirate* images for $l = 1$ and 2

| Wavelet Subbands | Values of the Kolmogorov-Smirnow metrics | | | | | |
|---|---|---|---|---|---|---|
| | Gaussian | | SNIG | | TSE | |
| | $M=4$ | $M=32$ | $M=4$ | $M=32$ | $M=4$ | $M=32$ |
| *Lena* | | | | | | |
| HL1 | **.0420** | .0454 | .0279 | .0189 | **.0278** | **.0082** |
| LH1 | .0431 | .0441 | .0300 | .0189 | **.0297** | **.0134** |
| HH1 | .0454 | .0426 | .0282 | .0183 | **.0297** | **.0151** |
| HL2 | .0476 | .0443 | **.0305** | .0195 | .0306 | **.0154** |
| LH2 | .0472 | .0273 | .0370 | .0174 | **.0368** | **.0122** |
| HH2 | .0465 | .0323 | .0295 | .0224 | **.0289** | **.0139** |
| *Boat* | | | | | | |
| HL1 | .0364 | .0422 | .0265 | .0210 | **.0247** | **.0158** |
| LH1 | .0362 | .0458 | .0283 | .0147 | **.0261** | **.0101** |
| HH1 | .0323 | .0307 | .0252 | .0193 | **.0248** | **.0136** |
| HL2 | .0401 | .0390 | .0311 | .0165 | **.0294** | **.0151** |
| LH2 | .0427 | .0443 | .0321 | .0271 | **.0318** | **.0196** |
| HH2 | .0345 | .0400 | .0251 | .0224 | **.0247** | **.0171** |
| *Pirate* | | | | | | |
| HL1 | .0472 | .0419 | **.0358** | **.0191** | .0364 | .0206 |
| LH1 | .0455 | .0330 | **.0371** | .0199 | .0378 | **.0152** |
| HH1 | .0431 | .0466 | .0373 | .0196 | **.0372** | **.0147** |
| HL2 | .0390 | .0415 | .0301 | **.0145** | **.0300** | .0148 |
| LH2 | .0398 | .0476 | .0356 | .0162 | **.0352** | **.0159** |
| HH2 | .0398 | .0367 | **.0351** | .0192 | .0353 | **.0157** |

Figure 3.2: Empirical, TSE, SNIG and Gaussian distributions for the HL ($l$ =1) subband of the DWT coefficients for the (a) *Lena*, (b) *Boat*, and (c) *Pirate* images.
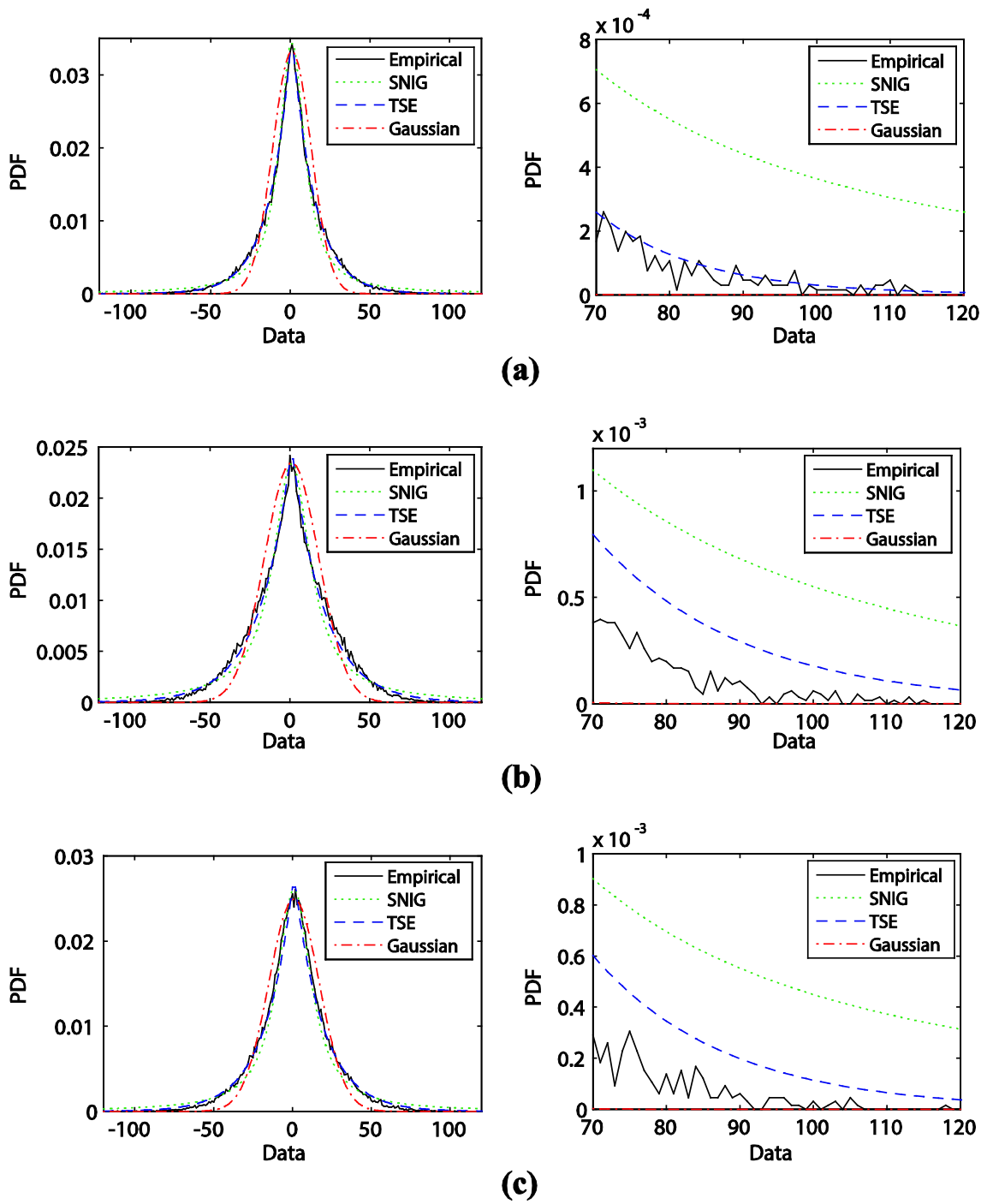
Figure 3.3: Empirical, TSE, SNIG and Gaussian distributions for the LH ($l$ =1) subband of the DWT coefficients for the (a) *Lena*, (b) *Boat*, and (c) *Pirate* images.
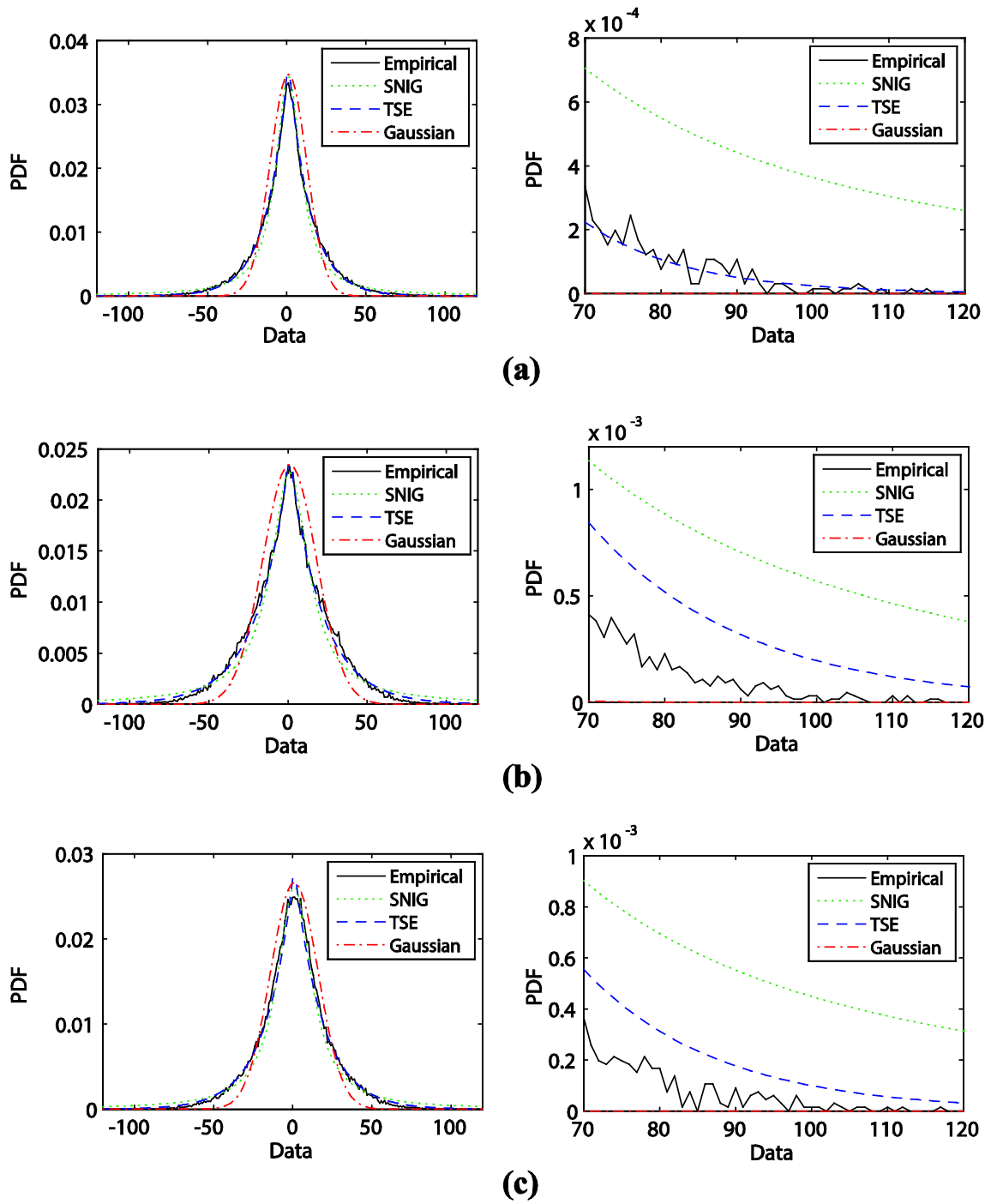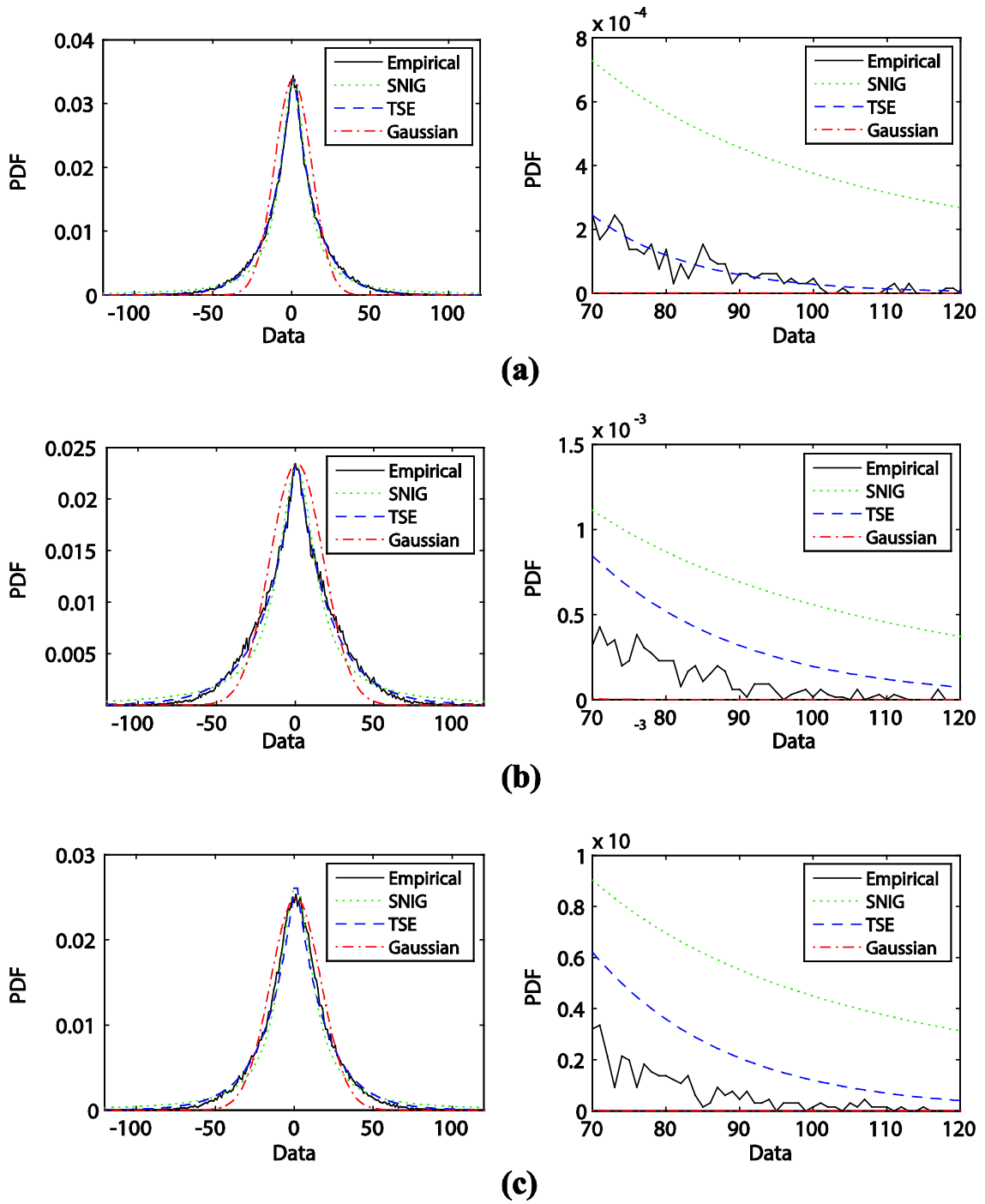
Figure 3.4: Empirical, TSE, SNIG and Gaussian distributions for the HH ($l$ =1) subband of the DWT coefficients for the (a) *Lena*, (b) *Boat*, and (c) *Pirate* images.

in general, provides a closer fit to the empirical distribution in comparison to that provided by the other two distributions coupled with the fact that it employs only one parameter, we use this distribution to model the DWT coefficients of the signal-dependant noise component of SAR images.

## 3.2.2 Modeling of the Reflectance Image

In this subsection, we provide a prior model for the wavelet coefficients of the reflectance component of SAR image, i.e., $x$. The characteristics of the distribution of the wavelet coefficients of an image have been studied by Mallat in [24]. It has been shown in his paper that, in general, the distribution of the wavelet image coefficients is symmetric and sharply-peaked at about zero with the tail being heavier than that of the Gaussian distribution. Achim *et al*. [13] have demonstrated that a sharply-peaked distribution with a tail heavier than that of the Gaussian distribution can be accurately modeled by a symmetric α-stable PDF. However, the alpha-stable PDF has a closed-form expression for only two specific values of its parameter α, namely, α =1 and α =2, resulting in the Cauchy and Gaussian PDFs respectively. It is worth mentioning that the employment of the α-stable PDF to model the wavelet coefficients without a closed-from expression increases the complexity of estimating numerically the noise-free wavelet coefficients. Thus, in view of the fact that the Gaussian PDF is not a suitable choice to model the wavelet coefficients of an image, in this work, the Cauchy PDF given by

$$p_x(x) = \frac{\gamma}{\pi(x^2 + \gamma^2)} \qquad (3.6)$$
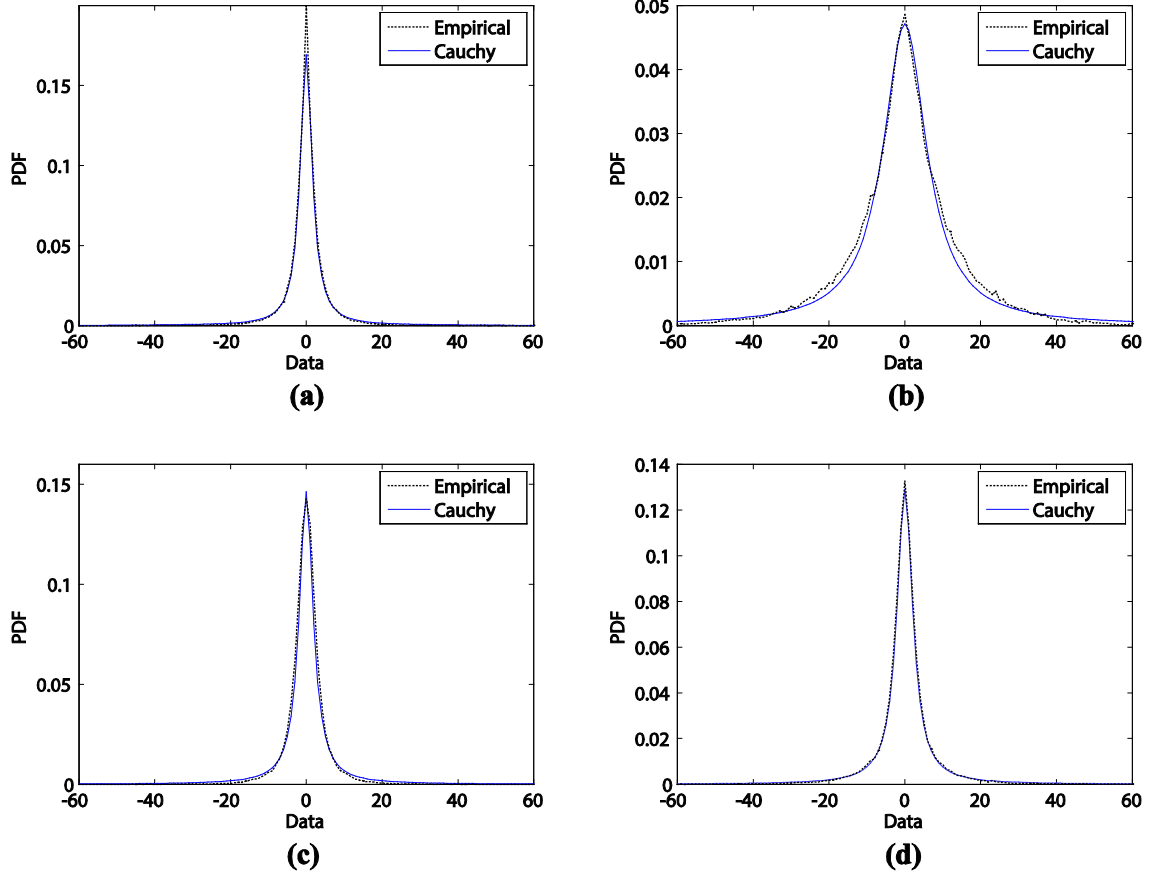
Figure 3.5: Empirical and Cauchy distributions for the HL ($l$ =1) subband of the DWT coefficients of the (a) *Lena*, (b) *Stream and Bridge*, (c) *Boat* and (d) *Pirate* images.

where $\gamma$ is the dispersion parameter, is adopted as a prior model for $x$. The modeling performance of the Cauchy PDF for the HL subband of the *Lena, Stream and Bridge, Boat* and *Pirate* images for $l = 1$ is depicted in Figure 3.5. It is obvious from this figure that the Cauchy PDF provides an excellent match to the empirical distribution both in the peak and tail parts.

Using the TSE and Cauchy PDFs to model the DWT coefficients of the signal-dependant noise and reflectance components, respectively, of an observed SAR image, a Bayesian estimation framework is devised to estimate the wavelet coefficients of the

speckle-free SAR image $x$. However, before proceeding to this part of our work, we first need to estimate the parameters of these distributions. In the next subsection we demonstrate the mechanisms used for estimating these parameters.

## 3.3 Estimation of $\beta$ and $\gamma$

In practical applications, the parameters $\beta$ and $\gamma$ need to be estimated from the observed noisy wavelet coefficients. Usually, the maximum likelihood (ML) method and the method of moments (MoM) are employed for the estimation of parameters. However, parameter estimation is, in general, a time-consuming process when using the former method [14], whereas it leads to a relatively large variance of the parameter estimated when using the latter one [22]. In [43], based on Mellin transform, a new method of parameter estimation, referred to as the method of second-kind cummulants or the method of log-cummulants (MoLC), has been proposed. It has been shown that this method is consistent and computationally efficient, and leads to a relatively low variance of the estimated parameter. We adopt this method to estimate the parameter $\beta$. However, it should be noted that MoLC is applicable only to positive-valued random variables. Therefore, in view of this and the fact that the TSE distribution is symmetric about zero and the histogram of the wavelet coefficients of the signal-dependant noise is approximately symmetric about zero, we estimate $\beta$ from the exponential distribution having the same parameter as that of TSE using the absolute value of the wavelet coefficients of the signal-dependant noise. The MoLC uses the traditional framework for the construction of moments and cummulants except that it replaces the Fourier transform with the Mellin transform. Thus, the n-th order second-kind cummulant of the exponential distribution is obtained as [43]

35

$$\hat{k}_{\mathrm{n}} = \frac{\mathrm{d^n}}{\mathrm{d}\varepsilon^{\mathrm{n}}} \varphi(\varepsilon)|_{\varepsilon=1} \qquad (3.7)$$

where $\varphi(\varepsilon)$ is the second second-kind characteristic function of the exponential distribution given by

$$\varphi(\varepsilon) = \log\left\{\int_0^\infty 2\, p_n(n)\, n^{\varepsilon-1}\mathrm{d}n\right\} = \log\left\{\int_0^\infty \frac{1}{\beta}\, \exp\left\{-\frac{n}{\beta}\right\} n^{\varepsilon-1}\mathrm{d}n\right\} \qquad (3.8)$$

In the above equation, $p_n(n)$ represents the TSE distribution of the signal-dependent noise wavelet coefficients $n$ in the range $[0, \infty)$. The table of integrations in [44] can be used to solve the integration in (3.8), yielding

$$\varphi(\varepsilon) = \log\left\{\beta^{\varepsilon-1}\Gamma(\varepsilon)\right\} \qquad (3.9)$$

where the symbol $\Gamma$ represents the Gamma function of the associated argument. By using (3.9) in (3.7), the first second-kind cummulant of the exponential distribution can be obtained as

$$\hat{k}_1 = \mathcal{D}(1) + \log(\beta) = -\Upsilon + \log(\beta) \qquad (3.10)$$

where $\mathcal{D}(\cdot)$ is the Digamma function and $\Upsilon$ is the Euler-Mascheroni constant [39]. Now, in order to estimate $\beta$, we compute the first second-kind cummulant $\tilde{\hat{k}}_1$ from the absolute values of the wavelet coefficients of the observed samples and use it as $\hat{k}_1$ in the above expression. As a result, the estimated $\tilde{\beta}$ is obtained by using the expression

$$\tilde{\beta} = \exp\left[\left\{\frac{1}{N_1 N_2}\sum_{p=1}^{N_1}\sum_{q=1}^{N_2} \log\left(y(p,q)\right)\right\} + \Upsilon\right] \qquad (3.11)$$

where $N_1$ and $N_2$ define the size $N_1 \times N_2$ of the wavelet subband considered.

Next, our task is to estimate the dispersion parameter $\gamma$ of the Cauchy distribution used to model the wavelet coefficients of the noise-free signal. It is to be noted that in order

36

to estimate the parameter $\beta$ of the signal-dependant noise $u$ using MoLC, we did use the noisy observation $g$. However, the same strategy of employing noisy observation cannot be used in MoLC in order to estimate the parameter $\gamma$, since $g$ is a noisy observation whereas $v$ is noise-free. It means that we cannot use $\tilde{k}_1$ as the first second-kind cummulant of the Cauchy distribution. Therefore, we propose to estimate the Cauchy distribution parameter $\gamma$ using the method proposed in [15]. In this method, the noisy observation is used to estimate the parameter $\gamma$ by minimizing the function

$$\int_{-\infty}^{\infty} \left| \widehat{\phi}_y(t) - \phi_y(t) \right| \exp(-t^2)\, dt \tag{3.12}$$

where $\widehat{\phi}_y(t)$ is the empirical characteristic function corresponding to the wavelet coefficients $y$ of the noisy observation, $\phi_y(t) = \phi_x(t)\, \phi_\epsilon(t)$, $\phi_x(t) = \exp(-\gamma|t|)$, and $\phi_\epsilon(t) = \exp(-(\sigma_\epsilon^2/2)|t|^2)$ with the standard deviation $\sigma_\epsilon$ obtained as [9]

$$\sigma_\epsilon = \frac{\mathrm{MAD}\left(y^{[1,4]}(\wp, \mathcal{q})\right)}{0.6745} \tag{3.13}$$

In (3.13), $\mathrm{MAD}$ denotes the median absolute deviation operation. The integral in (3.12) is calculated using the Gauss-Hermite quadrature as [15]

$$\sum_{d=1}^{Q} \vartheta_d \left| \widehat{\phi}_y(t_d) - \phi_y(t_d) \right| \tag{3.14}$$

where $t_d$'s are the roots of the Hermite polynomials of order $Q$, and $\vartheta_d$'s are the weights associated with these roots.

## 3.4 Proposed MMSE Bayesian Shrinkage Function

In this section, our goal is to formulate a shrinkage function under the framework of MMSE Bayesian estimation and to provide a realization for this function in order to estimate the noise-free wavelet coefficients of speckled images. This shrinkage function is formulated by employing the TSE and the Cauchy distributions as models for the wavelet coefficients of the signal-dependant noise and reflectance image, respectively. A description of our proposed scheme for despeckling is presented as an algorithm at the end of this section.

### 3.4.1 Formulation of a Shrinkage Function

Based on the Bayesian decision theory, the values of Bayes estimates $\tilde{x}$ of the noise-free wavelet coefficients $x$ of a subband, under the quadratic loss function, are given by the shrinkage function [45]:

$$\tilde{x}(y) = \int p_{x|y}(x|y)\, x\, dx \tag{3.15}$$

where $p_{x|y}(x|y)$ is the posterior density function conditioned on the observed wavelet coefficients $y$ of the subband considered. It is noted from (3.15) that this is simply the mean of $x$ conditioned on $y$. This estimation is achieved by carrying out a minimization of the mean square error (MSE) between $x$ and $\tilde{x}$. The posterior density function $p_{x|y}(x|y)$ can be obtained using the Bayes' rule as

$$p_{x|y}(x|y) = \frac{p_{y|x}(y|x)\, p_x(x)}{\int p_{y|x}(y|x)\, p_x(x)\, dx} = \frac{p_n(y-x)\, p_x(x)}{\int p_n(y-x)\, p_x(x)\, dx} \tag{3.16}$$

and hence, the shrinkage function $\tilde{x}\,(y)$ given by (3.15) can be re-written as

$$\tilde{x}(y) = \frac{\int p_n(y - x)p_x(x)\, x\, dx}{\int p_n(y - x)\, p_x(x)\, dx} \tag{3.17}$$

## 3.4.2  Realization of the Shrinkage Function

It is noted that a closed-form expression for $\tilde{x}(y)$ given by the above equation does not exist. Thus, in order to obtain the Bayesian estimates for the noise-free wavelet coefficients, the two integrations associated with (3.17) are numerically performed for each wavelet coefficient. Since this procedure requires an excessive computational effort, the discrete fast Fourier transform (DFT) has been employed due to its computational advantage [46]. The computational complexity of the direct numerical integration depends on the number of sample points used to perform the integration whereas that of DFT depends on the number of discrete points of $y$ resulting from choosing a certain bin-width. For a bin-width $\Delta y$, the number of discrete points of $y$ is given as $N_y = (y_{max} - y_{min})/\Delta y$, where $y_{max}$ and $y_{min}$ are, respectively, the maximum and minimum values of $y$. It should be noted that the computational complexity of the direct numerical integration and that of the DFT are reduced by utilizing a fewer number of sample points and a larger bin-width $\Delta y$, respectively. However, this is done at the expense of the estimation accuracy. Therefore, there is a need to investigate alternative realizations of the shrinkage function given by (3.17) for estimating the wavelet coefficients from the standpoint of the accuracy and computational complexity of the estimation. In order to achieve this goal, we now explore a representation for the shrinkage function given by (3.17) in which the associated integrals are replaced by infinite series. Substituting the expressions for $p_n(\cdot)$ and $p_x(\cdot)$ given by (3.4) and (3.6), respectively, into (3.17), we have

$$\tilde{x}\,(y) = \frac{\int_{-\infty}^{\infty} \frac{e^{\frac{-|-x+y|}{\beta}}}{x^2 + \gamma^2}\, x\, dx}{\int_{-\infty}^{\infty} \frac{e^{\frac{-|-x+y|}{\beta}}}{x^2 + \gamma^2}\, dx} = \frac{A(y)}{B(y)} \qquad (3.18)$$

where $A(y)$ and $B(y)$ are, respectively, the numerator and denominator of the shrinkage

function $\tilde{x}\,(y)$, and they are given by

$$A(y) \;=\; \int_{-\infty}^{\infty} \frac{e^{\frac{-|-x+y|}{\beta}}}{x^2 + \gamma^2}\, x\, dx$$

$$= e^{\frac{-y}{\beta}} \int_{-\infty}^{y} \frac{e^{\frac{x}{\beta}}}{x^2 + \gamma^2}\, x\, dx + e^{\frac{y}{\beta}} \int_{y}^{\infty} \frac{e^{\frac{-x}{\beta}}}{x^2 + \gamma^2}\, x\, dx \qquad (3.19)$$

$$B(y) \;=\; \int_{-\infty}^{\infty} \frac{e^{\frac{-|-x+y|}{\beta}}}{x^2 + \gamma^2}\, dx$$

$$= e^{\frac{-y}{\beta}} \int_{-\infty}^{y} \frac{e^{\frac{x}{\beta}}}{x^2 + \gamma^2}\, dx + e^{\frac{y}{\beta}} \int_{y}^{\infty} \frac{e^{\frac{-x}{\beta}}}{x^2 + \gamma^2}\, dx \qquad (3.20)$$

By assuming that $y \leq 0$, the expressions for $A(y)$ and $B(y)$ as given above can be further

manipulated to yield

$$A(y) = e^{\frac{-y}{\beta}} \left[ \int_{-\infty}^{0} \frac{e^{\frac{x}{\beta}}}{x^2 + \gamma^2}\, x\, dx - \int_{y}^{0} \frac{e^{\frac{x}{\beta}}}{x^2 + \gamma^2}\, x\, dx \right]$$

$$+ e^{\frac{y}{\beta}} \left[ \int_{y}^{0} \frac{e^{\frac{-x}{\beta}}}{x^2 + \gamma^2}\, x\, dx + \int_{0}^{\infty} \frac{e^{\frac{-x}{\beta}}}{x^2 + \gamma^2}\, x\, dx \right]$$

$$= e^{\frac{-y}{\beta}} \left[ - \int_{0}^{\infty} \frac{e^{\frac{-x}{\beta}}}{x^2 + \gamma^2}\, x\, dx + \int_{0}^{y} \frac{e^{\frac{x}{\beta}}}{x^2 + \gamma^2}\, x\, dx \right]$$

$$+ e^{\frac{y}{\beta}} \left[ -\int_0^y \frac{e^{\frac{-x}{\beta}}}{x^2 + \gamma^2} \, x \, dx + \int_0^\infty \frac{e^{\frac{-x}{\beta}}}{x^2 + \gamma^2} \, x \, dx \right] \qquad (3.21)$$

$$B(y) = e^{\frac{-y}{\beta}} \left[ \int_{-\infty}^0 \frac{e^{\frac{x}{\beta}}}{x^2 + \gamma^2} \, dx - \int_y^0 \frac{e^{\frac{x}{\beta}}}{x^2 + \gamma^2} \, dx \right]$$

$$+ e^{\frac{y}{\beta}} \left[ \int_y^0 \frac{e^{\frac{-x}{\beta}}}{x^2 + \gamma^2} \, dx + \int_0^\infty \frac{e^{\frac{-x}{\beta}}}{x^2 + \gamma^2} \, dx \right]$$

$$= e^{\frac{-y}{\beta}} \left[ \int_0^\infty \frac{e^{\frac{-x}{\beta}}}{x^2 + \gamma^2} \, dx + \int_0^y \frac{e^{\frac{x}{\beta}}}{x^2 + \gamma^2} \, dx \right]$$

$$+ e^{\frac{y}{\beta}} \left[ -\int_0^y \frac{e^{\frac{-x}{\beta}}}{x^2 + \gamma^2} \, dx + \int_0^\infty \frac{e^{\frac{-x}{\beta}}}{x^2 + \gamma^2} \, dx \right] \qquad (3.22)$$

It can be shown that one would obtain exactly the same expression for $A(y)$ or $B(y)$ as given above even when $y > 0$. Now, by substituting (3.21) and (3.22) in (3.18), $\tilde{x}(y)$ can be expressed as

$$\tilde{x}(y) = \frac{e^{\frac{-y}{\beta}}[f_{11}(y) - \eta_1] + e^{\frac{y}{\beta}}[-f_{12}(y) + \eta_1]}{e^{\frac{-y}{\beta}}[f_{21}(y) + \eta_2] + e^{\frac{y}{\beta}}[-f_{22}(y) + \eta_2]} \qquad (3.23)$$

where

$$f_{11}(y) = f_{12}(-y) = \int_0^y \frac{e^{\frac{x}{\beta}}}{x^2 + \gamma^2} \, x \, dx, \qquad (3.24)$$

$$f_{21}(y) = -f_{22}(-y) = \int_0^y \frac{e^{\frac{x}{\beta}}}{x^2 + \gamma^2} \, dx, \qquad (3.25)$$

$$\eta_1 = \int_0^\infty \frac{e^{\frac{-x}{\beta}}}{x^2 + \gamma^2} \, x \, dx \, , \text{ and} \tag{3.26}$$

$$\eta_2 = \int_0^\infty \frac{e^{\frac{-x}{\beta}}}{x^2 + \gamma^2} \, dx \tag{3.27}$$

Since $\beta$ and $\gamma$ are real, using the tool in [47], the above four integrals can be written as

$$f_{11}(y) = \sin\left(\frac{\gamma}{\beta}\right)\left[\mathrm{Im}\left\{E_1\left(\frac{-y + \mathrm{j}\gamma}{\beta}\right)\right\} - \mathrm{Si}(\frac{\gamma}{\beta}) + \frac{\pi}{2}\right]$$

$$- \cos\left(\frac{\gamma}{\beta}\right)\left[\mathrm{Re}\left\{E_1\left(\frac{-y + \mathrm{j}\gamma}{\beta}\right)\right\} + \mathrm{Ci}(\frac{\gamma}{\beta})\right] \tag{3.28}$$

$$\eta_1 = \lim_{y \to \infty} f_{12}(y) = \sin\left(\frac{\gamma}{\beta}\right)\left[-\mathrm{Si}(\frac{\gamma}{\beta}) + \frac{\pi}{2}\right] - \cos\left(\frac{\gamma}{\beta}\right)\left[\mathrm{Ci}(\frac{\gamma}{\beta})\right] \tag{3.29}$$

$$f_{21}(y) = -\frac{1}{\gamma}\sin\left(\frac{\gamma}{\beta}\right)\left[\mathrm{Re}\left\{E_1\left(\frac{-y + \mathrm{j}\gamma}{\beta}\right)\right\} + \mathrm{Ci}(\frac{\gamma}{\beta})\right]$$

$$- \frac{1}{\gamma}\cos\left(\frac{\gamma}{\beta}\right)\left[\mathrm{Im}\left\{E_1\left(\frac{-y + \mathrm{j}\gamma}{\beta}\right)\right\} - \mathrm{Si}(\frac{\gamma}{\beta}) + \frac{\pi}{2}\right] \tag{3.30}$$

$$\eta_2 = \lim_{y \to \infty} f_{22}(y) = \frac{1}{\gamma}\sin\left(\frac{\gamma}{\beta}\right)\left[\mathrm{Ci}(\frac{\gamma}{\beta})\right] + \frac{1}{\gamma}\cos\left(\frac{\gamma}{\beta}\right)\left[-\mathrm{Si}(\frac{\gamma}{\beta}) + \frac{\pi}{2}\right] \tag{3.31}$$

where $\mathrm{j} = \sqrt{-1}$, $\mathrm{Re}\{\cdot\}$ and $\mathrm{Im}\{\cdot\}$ are the real and imaginary parts, respectively, of the associated complex argument, and $E_1(\cdot)$, $\mathrm{Si}(\cdot)$ and $\mathrm{Ci}(\cdot)$ are, respectively, the exponential, sine and cosine integral functions defined as [39]

$$E_1(\mathfrak{z}) = \int_{\mathfrak{z}}^\infty \frac{e^{-w}}{w} \, dw = -\Upsilon - \ln(\mathfrak{z}) - \sum_{q=1}^\infty \frac{(-\mathfrak{z})^q}{q \, q!}, \qquad |\mathrm{Arg}\{\mathfrak{z}\}| \le \pi \tag{3.32}$$

$$\mathrm{Si}(\mathfrak{z}) = \int_1^{\mathfrak{z}} \frac{\sin(w)}{w} \, dw = \sum_{q=1}^\infty \frac{(-1)^{q-1}\mathfrak{z}^{2q-1}}{(2q-1)(2q-1)!} \tag{3.33}$$

$$\text{Ci}(\mathfrak{z}) = \Upsilon + \ln(\mathfrak{z}) + \int_0^\mathfrak{z} \frac{\cos(w) - 1}{w} \, dw = \Upsilon + \ln(\mathfrak{z}) + \sum_{q=1}^{\infty} \frac{(-1)^q \mathfrak{z}^{2q}}{(2q)(2q)!} \quad \textbf{(3.34)}$$

$\mathfrak{z}$ being a complex number.

The computational complexity of estimating the wavelet coefficients in a subband using the shrinkage function given by (3.23) is $O(2(C_{f_{11}} + C_{f_{21}})N_1 N_2)$, where $C_{f_{11}}$ and $C_{f_{21}}$ are the computational complexities of $f_{11}(\cdot)$ and $f_{21}(\cdot)$, respectively. Since the computational complexities $C_{f_{11}}$ and $C_{f_{21}}$ depend entirely on the complexity of calculating $E_1(\cdot)$, $\text{Si}(\cdot)$ and $\text{Ci}(\cdot)$, using a fewer number of terms of the infinite series given by (3.32), (3.33) and (3.34) reduces the computational effort needed in estimating the wavelet coefficients using the shrinkage function given by (3.23).

In order to study both the estimation accuracy of the wavelet coefficients and the computational efforts associated with the estimation using the direct numerical integration, DFT and the shrinkage function given by (3.23), we implement the three procedures using MATLAB codes on a 2.9-GHz 8-GB machine. For this experiment, we implement these three procedures to estimate the noise-free DWT coefficients at $l = 1$ for each of the HL, LH and HH subbands of the *Lena*, *Boat* and *Pirate* images that are synthetically-contaminated by two different strengths of the speckle noise, namely, for $M = 32$ and $M = 14$. We now study the time complexity of the three realizations of the shrinkage function in providing the same level of the estimation accuracy by them. For this purpose, we implement each of the three realizations of the shrinkage function independently and observe the time complexity in achieving a steady-state in the first three decimal places of the value of an estimated wavelet coefficient. We measure the execution times of the three

43

Table 3.2: Average execution times, in milliseconds, of three different procedures for estimating a wavelet coefficient with a precision of three decimal digits

| Estimation procedure | Direct numerical integration | DFT | Equation (3.23) |
| --- | --- | --- | --- |
| Execution time in milliseconds | 57.395 | 4.748 | 0.785 |

realizations, by using the minimum number of grid points along the $x$-axis in the direct numerical integration realization, the minimum number of sample points of $y$ in the DFT realization and the minimum number of terms in the infinite series in the proposed realization, that lead to the steady-state values of the estimated wavelet coefficient of the three realizations. Table 3.2 gives the execution time of each of the three realizations. The execution time given in this table is the time of computing a single DWT coefficient averaged over all the DWT coefficients in the HL, LH and HH subbands of the three images. It is observed from this table that the proposed realization of the shrinkage function given by (3.23) requires a substantially reduced computational effort in comparison to that required by using either the direct numerical integration realization or the DFT realization. Figures 3.6, 3.7 and 3.8 show the plots of the shrinkage function obtained by the three realizations, for the HL, LH and HH subbands, respectively, of the *Lena*, *boat* and *pirate* images for $M = 32$ and $M = 14$. It is seen from these figures that the plots of the three realizations overlap one another over the entire spectrum of the values of the noisy coefficients indicating that the three realizations achieve the same estimation accuracy.

In view of this study, which shows that the shrinkage function realized by using (3.23) requires lower computational time than that required by using the direct numerical integration or DFT, the proposed realization of the shrinkage function is adopted for

Figure 3.6: Estimated HL-subband wavelet coefficients obtained from the shrinkage function realized by the direct numerical integration, DFT and proposed technique.

Figure 3.7: Estimated LH-subband wavelet coefficients obtained from the shrinkage function realized by the direct numerical integration, DFT and proposed technique.
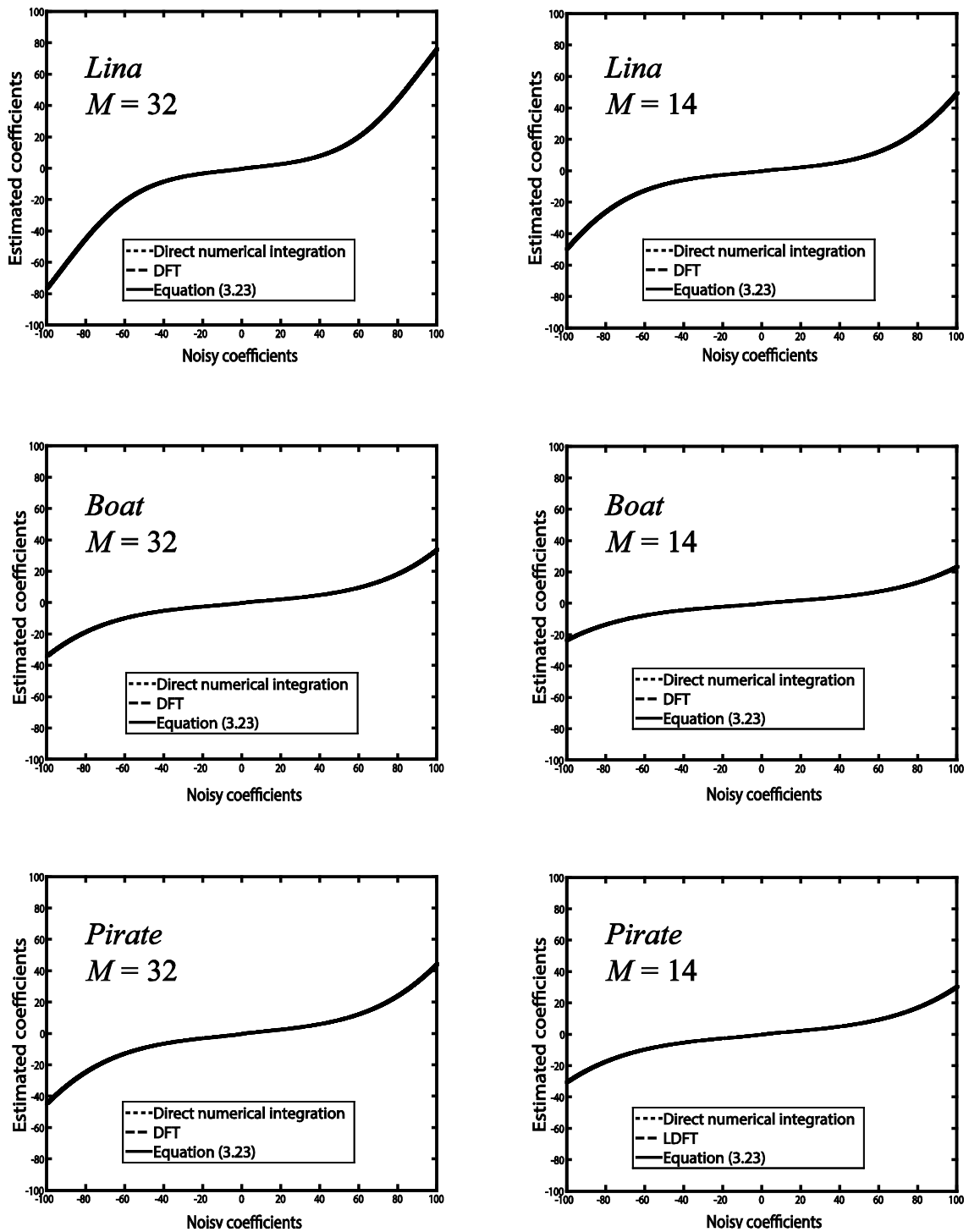
Figure 3.8: Estimated HH-subband wavelet coefficients obtained from the shrinkage function realized by the direct numerical integration, DFT and proposed technique.
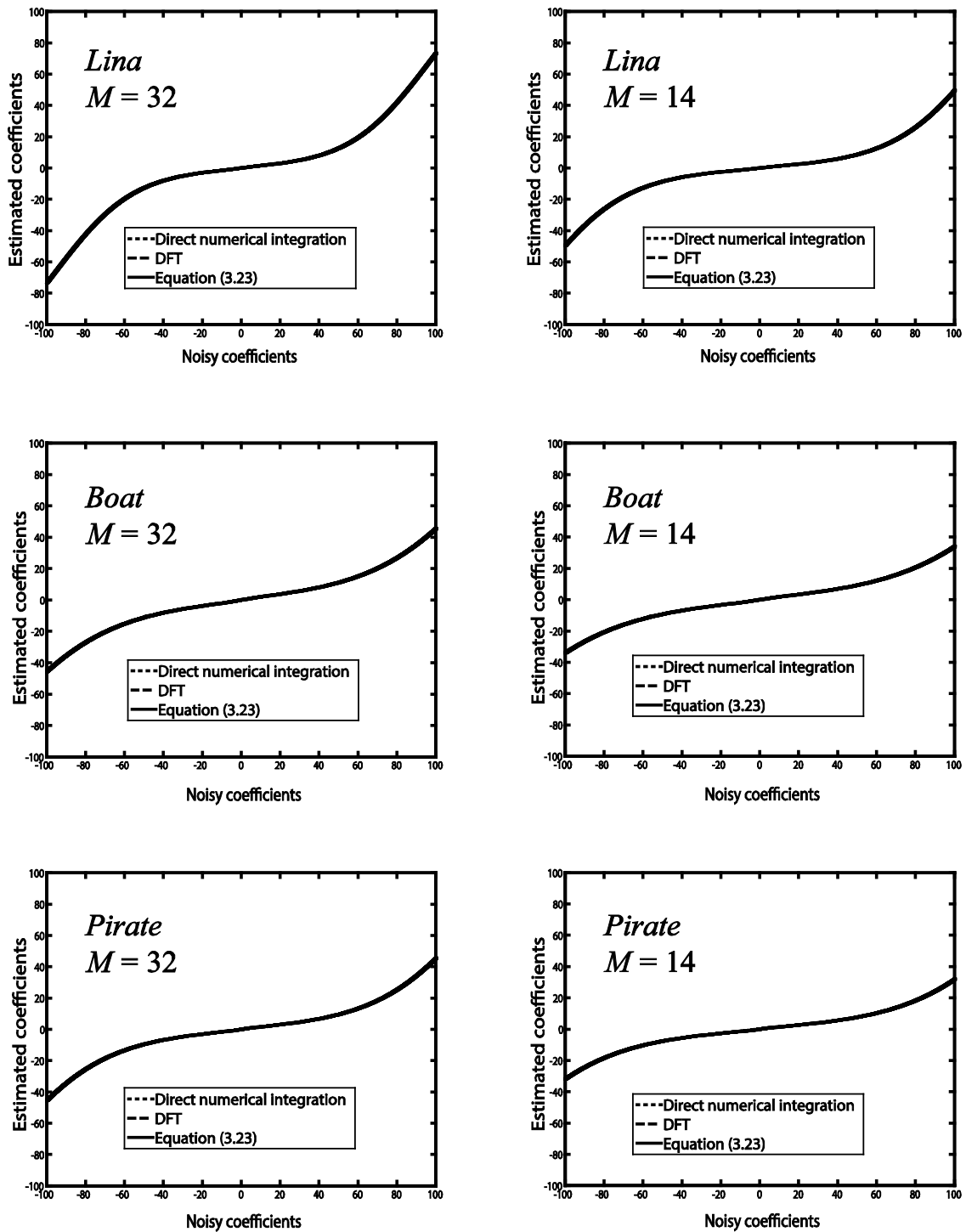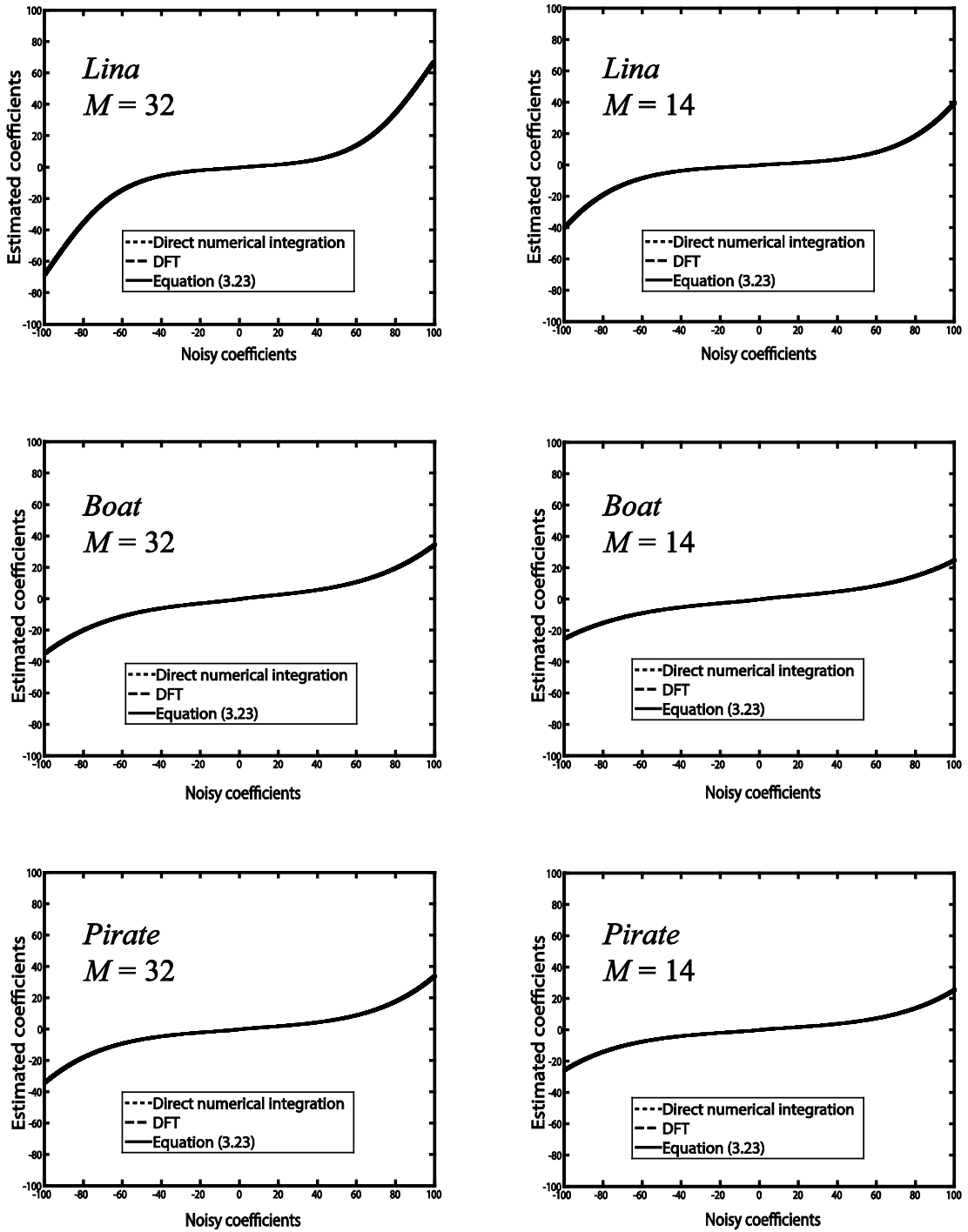
obtaining the Bayesian estimates of the wavelet coefficients in our algorithm for despeckling of images.

### 3.4.3 Steps of the Proposed Algorithm

The proposed scheme for despeckling can be summarized as follows.

1) Carry out the DWT on the observed image at decomposition levels $l = 1, 2, 3, \cdots \log_2(\mathcal{N})$, where $\mathcal{N}$ defines the size $\mathcal{N} \times \mathcal{N}$ of the image.

2) Estimate the parameters $\beta$ and $\gamma$ corresponding to each detail subband, namely, HL, LH and HH, for each level of decomposition by using (3.11) and (3.12), respectively.

3) Obtain the estimated noise-free wavelet coefficients for each detail subband using the MMSE Bayesian shrinkage function realized by (3.23).

4) Perform the inverse DWT of the coefficients obtained in step 3.

## 3.5 Summary

In this chapter, our objective has been to develop a Bayesian shrinkage function with a low-complexity realization to estimate the noise-free wavelet coefficients of a speckled image. In order to meet this objective, suitable statistical models for the wavelet coefficients of the components of a speckled image, namely, the reflectance image and the signal-dependant noise, have been investigated. A study has been undertaken to investigate the suitability of a TSE distribution to model the wavelet coefficients of the signal-dependent noise. It has been demonstrated that the TSE distribution is capable of accurately modeling the wavelet coefficients of this component of a speckled image. A Cauchy PDF has been selected to be the prior distribution of the wavelet coefficients of the reflectance image, since this PDF is proven to be a good model for these coefficients. The TSE and Cauchy distributions have been employed to formulate a MMSE Bayesian shrinkage

function to obtain the estimates of the noise-free wavelet coefficients. A low-complexity, yet accurate, realization of this shrinkage function has been then devised, and its efficacy from the standpoint of accuracy as well as computational cost has been verified. Finally, the steps of the proposed algorithm for despeckling has been given.

# CHAPTER 4
# Experimental Results

## 4.1 Introduction

In the previous chapter, a wavelet-based Bayesian shrinkage function was developed to estimate the noise-free wavelet coefficients of a speckled image, and this shrinkage function was used in our proposed despeckling scheme. In this chapter, extensive experimentations are conducted to study the performance of the proposed despeckling scheme. In the implementation of the proposed scheme, the Daubechies' *Symlet* wavelet with $N_v = 8$ is used and the value of $Q$ in (3.16) is chosen to be 20. The performance of the new scheme is compared with those of some of other despeckling schemes available in the literature, namely, the schemes of using soft thresholding (S-Threshold) [9], Bayes-shrink soft thresholding (B-Shrink) [48], Lee filter (Lee-F) [2], the spatially-adaptive wavelet-based shrinkage function (SA-WBMMAE) [15] and adaptive nonlocal filtering (SARBM3D) [49]. The first three of these schemes are extremely fast whereas the other two schemes are known to provide very competitive performances. The codes for these various schemes are readily available either online or upon a request to the authors of the papers [50-52]. Experiments using all the despeckling schemes are performed on both synthetically speckled images and real SAR images. It is to be noted that the parameters in

all the algorithms used for comparison are those suggested by their authors for their best performances.

## 4.2 Synthetically-degraded Images

In this section, our goal is to study the performances of the various despeckling schemes when applied to synthetically speckled images. Two images commonly used in the literature, namely *Lena* and *Stream and Bridge*, are subjected to synthetically generated speckle noise at different levels, as described in Chapter 3. These images comprise 512×512 pixels. The metric signal-to-noise ratio (SNR) [12] is used to measure the performances of the various despeckling schemes. This metric provides an indication of the ability of a scheme in reducing the level of noise. However, it is shown in [12] that SNR is not sufficiently consistent with human perception of an image, since it does not fully reflect the visual quality of the image. Therefore, in our performance evaluation of the despeckling schemes, we also consider some other metrics that are representatives of some other aspects of human visual perception of an image.

One such metric is the measure of structural similarity (SSIM) [53] that compares the local patterns of the pixel intensities between the original and processed images normalized for their luminance and contrast. If $X$ and $\tilde{X}$ represent, respectively, the original and processed images with $\mu_X$ and $\mu_{\tilde{X}}$, as pixel means, and $\sigma_X^2$ and $\sigma_{\tilde{X}}^2$ as pixel variances of the respective images, then SSIM is defined as [53]

$$\text{SSIM}(X,\tilde{X}) = \frac{(2\mu_X\mu_{\tilde{X}} + C_1)(2\Sigma_{X\tilde{X}} + C_2)}{(\mu_X^2 + \mu_{\tilde{X}}^2 + C_1)(\sigma_X^2 + \sigma_{\tilde{X}}^2 + C_2)} \qquad \textbf{(4.1)}$$

where $\Sigma_{X\tilde{X}}$ is the covariance of $X$ and $\tilde{X}$, $C_1 = (0.01\mathcal{L})^2$ and $C_2 = (0.02\mathcal{L})^2$, $\mathcal{L}$ being the dynamic range of the pixel values. In our experiments, we have $\mathcal{L} = 2^8\text{-}1$.

The homogeneity $\mathcal{H}$ and correlation $\mathcal{C}$ of the pixel values of an image can be used to describe its texture [41]. These two features are defined using the normalized co-occurrence matrix $\mathcal{P}$ as [41]

$$\mathcal{H} = \frac{\sum_{i=1}^{\mathcal{L}+1} \sum_{j=1}^{\mathcal{L}+1} \mathcal{P}(i,j)}{1 + |i-j|} \tag{4.2}$$

$$\mathcal{C} = \frac{\sum_{i=1}^{\mathcal{L}+1} \sum_{j=1}^{\mathcal{L}+1} (ij)\,\mathcal{P}(i,j) - \mu_v \mu_w}{\sigma_v \sigma_w} \tag{4.3}$$

where $\mathcal{P}(i,j)$ is the value of $(i,j)$th entry in the normalized co-occurrence matrix and $\mu_v$, $\sigma_v$ and $\mu_w$,$\sigma_w$ are the means and standard deviations of the elements of the column vectors $\mathcal{P}_v$ and $\mathcal{P}_w$ defined as

$$\mathcal{P}_v(i) = \sum_{j=1}^{\mathcal{L}+1} \mathcal{P}(i,j) \tag{4.4}$$

$$\mathcal{P}_w(j) = \sum_{i=1}^{\mathcal{L}+1} \mathcal{P}(i,j) \tag{4.5}$$

The difference in the homogeneity, $\Delta\mathcal{H}$, and the difference in the correlation, $\Delta\mathcal{C}$, between the original and the processed images can be used as metrics of quantifying the ability of a despeckling scheme in preserving the texture of the original image in the processed one. These metrics are used as a measure of texture preservation in our performance evaluation of the despeckling schemes.

It is to be noted that all the metrics mentioned above emphasize on measuring the performances of the various despeckling schemes from the perspectives of speckle-removal and preservation of the original features of the image without taking into account

the associated computational cost. Thus, in order to obtain a reasonable comparison between the various despeckling schemes, the computer execution times of running the various despeckling algorithms are also taken into consideration.

The results of SNR, SIMM, $\Delta\mathcal{H}$ and $\Delta\mathcal{C}$ obtained for the *Lena* and *Stream and Bridge* images are shown in Tables 4.1 and 4.2, respectively, for three different strengths of the speckle noise, namely, for $M = 4$, 32 and 64. These two tables demonstrate that, in terms of the SNR measure, the proposed scheme outperforms the S-Threshold, B-Shrink and Lee-F schemes with the difference in SNR values ranging from 0.87 dB to 5.63 dB whereas it is outperformed by SA-WBMMEA and SARBM3D schemes with 0.11 dB to 1.81 dB difference. However, it is to be noted that the proposed scheme yields a noticeable difference in the SNR values from those provided by SA-WBMMEA and SARBM3D schemes only for very high levels of speckle noise but not so when the strength of the speckle noise is low or medium. On the other hand, the proposed scheme yields a significantly higher SNR values compared with that provided by the remaining schemes irrespective of the levels of the speckle noise. With regard to the SSIM values for the various schemes, it is seen from the two tables that the performance of the proposed scheme is competitive to that of the SA-WBMMEA and SARBM3D schemes, but it is much superior to that of the other three schemes. In terms of the measures of $\Delta\mathcal{H}$ and $\Delta\mathcal{C}$, it is clearly evident from their values given in the two tables that the proposed scheme provides almost invariably the best performance indicating its superiority in preserving the original image textures in the despeckled image.

53

Table 4.1: Results of applying various despeckling schemes to synthetically corrupted *Lena* image with different strengths of speckle noise

| Despeckling scheme | $M = 4$, SNR=-5.36 dB | | | | $M = 32$, SNR=14.2 dB | | | | $M = 64$, SNR=27.01 dB | | | |
|---|---|---|---|---|---|---|---|---|---|---|---|---|
| | SNR | SSIM | $\Delta\mathcal{H}$ | $\Delta\mathcal{C}$ | SNR | SSIM | $\Delta\mathcal{H}$ | $\Delta\mathcal{C}$ | SNR | SSIM | $\Delta\mathcal{H}$ | $\Delta\mathcal{C}$ |
| S-Threshold | 10.98 | 0.4015 | 0.0249 | 0.0237 | 26.23 | 0.6027 | 0.0200 | 0.0207 | 32.03 | 0.7791 | 0.0109 | 0.0118 |
| B-Shrink | 12.89 | 0.5013 | 0.0317 | 0.0212 | 28.14 | 0.6981 | 0.0119[2] | 0.081[2] | 33.64 | 0.8211 | 0.0076[3] | 0.0063[2] |
| Lee-F | 12.21 | 0.4147 | 0.0271 | 0.0190 | 27.87 | 0.6731 | 0.0221 | 0.0091[3] | 32.28 | 0.8279 | 0.0051[2] | 0.0070[3] |
| SAWBMMEA | 14.82[2] | 0.5874[2] | 0.0231[2] | 0.0168[2] | 32.47[2] | 0.7689[2] | 0.0209[3] | 0.0144 | 37.97[2] | 0.8631[3] | 0.0195 | 0.0136 |
| SARBM3D | 15.57[1] | 0.6461[1] | 0.0243[3] | 0.0183[3] | 32.92[1] | 0.7908[1] | 0.0232 | 0.0158 | 38.12[1] | 0.8730[1] | 0.0218 | 0.0149 |
| *Proposed* | 13.76[3] | 0.5370[3] | 0.0172[1] | 0.0081[1] | 31.46[3] | 0.7512[3] | 0.0091[1] | 0.0061[1] | 37.66[3] | 0.8634[2] | 0.0046[1] | 0.0033[1] |

[1] First best, [2] Second best, [3] Third best.

54

Table 4.2: Results of applying various despeckling schemes to synthetically corrupted *Stream and Bridge* image with different strengths of speckle noise

| Despeckling scheme | $M = 4$, SNR=-5.92 dB | | | | $M = 32$, SNR=13.1 dB | | | | $M = 64$, SNR=24.61 dB | | | |
|---|---|---|---|---|---|---|---|---|---|---|---|---|
| | SNR | SSIM | $\Delta\mathcal{H}$ | $\Delta\mathcal{C}$ | SNR | SSIM | $\Delta\mathcal{H}$ | $\Delta\mathcal{C}$ | SNR | SSIM | $\Delta\mathcal{H}$ | $\Delta\mathcal{C}$ |
| S-Threshold | 8.99 | 0.3018 | 0.0380[2] | 0.0402 | 24.27 | 0.5526 | 0.0234[2] | 0.0303 | 29.87 | 0.7528 | 0.0148[3] | 0.0160 |
| B-Shrink | 10.97 | 0.3484 | 0.0456 | 0.0339[2] | 25.62 | 0.5990 | 0.0298[3] | 0.0217[3] | 31.76 | 0.7641 | 0.0151 | 0.0144[3] |
| Lee-F | 9.64 | 0.3074 | 0.0585 | 0.0355 | 24.01 | 0.5732 | 0.0377 | 0.0193[2] | 30.89 | 0.7583 | 0.0093[1] | 0.0092[2] |
| SAWBMMEA | 13.91[2] | 0.4912[2] | 0.0397[3] | 0.0354[3] | 28.09[2] | 0.6897[2] | 0.0378 | 0.0301 | 33.12[2] | 0.7971[3] | 0.0290 | 0.0287 |
| SARBM3D | 14.39[1] | 0.5456[1] | 0.0420 | 0.0376 | 28.51[1] | 0.7004[1] | 0.0380 | 0.0353 | 33.54[1] | 0.8024[2] | 0.0321 | 0.0348 |
| *Proposed* | 12.88[3] | 0.4412[3] | 0.0363[1] | 0.0324[1] | 27.22[3] | 0.6510[3] | 0.0196[1] | 0.0131[1] | 33.01[3] | 0.8025[1] | 0.0101[2] | 0.0085[1] |

[1] First best, [2] Second best, [3] Third best.

55

In order to relate the performances of the various despeckling schemes with the corresponding execution times, we compute the execution time needed to despeckle a noisy image using each despeckling scheme on a 2.9-GHz 8-GB machine. The execution times needed to despeckle the noisy *Lena* and *Stream and Bridge* images, each of sizes 256×256 and 512×512, using the various despeckling schemes are given in Table 4.3. It is observed from the execution times of the various algorithms given in this table that the time complexity of the proposed scheme is competitive to that of the S-Threshold and Lee-F schemes, at least one-third of that of the B-Shrink scheme and several orders of magnitude lower than that of SA-WBMMEA and SARBM3D schemes.

From the comparison of the various despeckling schemes carried out in this subsection, it can be concluded that the proposed scheme provides the best trade-off between the performance and the time complexity.

Figures 4.1 and 4.2 show the original and noisy ($M = 32$) versions of the *Lena* and *Stream and Bridge* images as well as the corresponding images despeckled by using the various despeckling schemes. It is seen from the images in these figures that the S-Threshold, B-Shrink and Lee-F schemes provide despeckled images that suffer from the presence of visually noticeable speckle noise. On the other hand, the SA-WBMMEA and SARBM3D schemes severely over-smooth the noisy images thus providing despeckled images in which some of the texture details are lost. However, the proposed despeckling scheme results in images with not only a reasonable reduction in the speckle noise but also a good preservation of the textures of the original images. The evidence of the superiority of the proposed scheme in obtaining the best visual quality of the processed image among

56

Table 4.3: Execution times (in seconds) of various despeckling schemes for the *Lena* and *Stream and Bridge* images

| Despeckling scheme | Execution times (in seconds) | |
| --- | --- | --- |
| | Image size | |
| | 256×256 | 512×512 |
| *Lena* | | |
| S-Threshold | **0.26**[3] | **0.34**[3] |
| B-Shrink | 0.85 | 1.03 |
| Lee-F | **0.18**[1] | **0.27**[2] |
| SAWBMMEA | 36.81 | 147.47 |
| SARBM3D | 97.97 | 311.8 |
| *Proposed* | **0.19**[2] | **0.26**[1] |
| *Stream and Bridge* | | |
| S-Threshold | **0.20**[3] | **0.27**[3] |
| B-Shrink | 0.52 | .91 |
| Lee-F | **0.17**[2] | **0.23**[1] |
| SAWBMMEA | 34.81 | 142.47 |
| SARBM3D | 81.47 | 289.8 |
| *Proposed* | **0.16**[1] | **0.24**[2] |

[1] First best, [2] Second best, [3] Third best.

Figure 4.1: Magnified versions of the *Lena* image. (a) Original. (b) Noisy, $M = 32$. Despeckled images using the (c) S-Threshold, (d) B-Shrink, (e) Lee-F, (f) SA-WBMMAE, (g) SARBM3D, and (h) Proposed schemes.
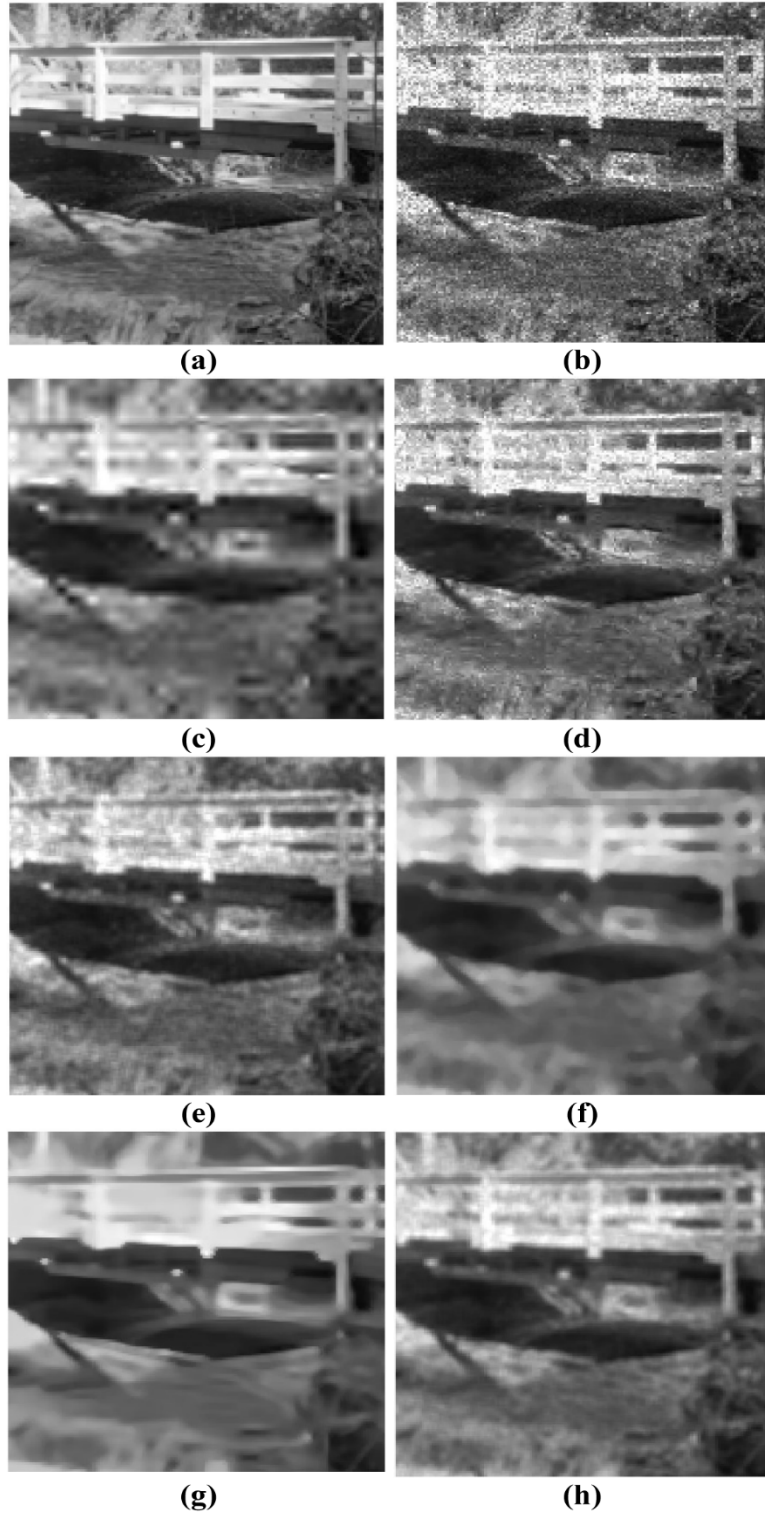
Figure 4.2: Magnified versions of the *Stream and Bridge* image. (a) Original. (b) Noisy, $M = 32$. Despeckled images using the (c) S-Threshold, (b) B-Shrink, (e) Lee-F, (f) SA-WBMMAE, (g) SARBM3D, and (h) Proposed schemes.

the various despeckling schemes is especially noticeable in some of the regions of the processed images shown in Figures 4.1 and 4.2. For example, it is seen that the creases in the hat of the *Lena* image and parts of the bridge in the *Stream and Bridge* image are apparently overwhelmed by the speckle noise still remaining in the images despeckled by the S-Threshold, B-Shrink and Lee-F schemes. On the other hand, these parts of the images are over-smoothed thus are not as clear or have disappeared in the images despeckled by the SA-WBMMEA and SARBM3D schemes. However, these parts are noticeably more clear in the images despeckled by the proposed scheme.

## 4.3  Real SAR Images

In this section, the proposed despeckling scheme is applied to real SAR images and the results are compared with that of the other schemes. Since for SAR images, noise-free images cannot be made available, in the experiments of this section, we use the *Mean* and the *equivalent number of looks* (ENL) values of the ratio image to measure the performance of the various despeckling schemes [54]. The *ratio image* is the ratio of the observed noisy image and the despeckled image. The *Mean* value is the arithmetic mean (average) of the pixel intensities of the ratio image, whereas the ENL value is the ratio of the square of the mean and the variance of the intensities of this image. If an ideal despeckling scheme could be applied to a SAR image with an $M$-look, the Mean and the ENL values as defined above should be equal to unity and $M$, respectively.

Two Terrasar-X SAR images [55], *Chile Copper Mine* and *Panama Canal*, captured by the satellite imagery of Airbus Defence and Space [56] are used in our
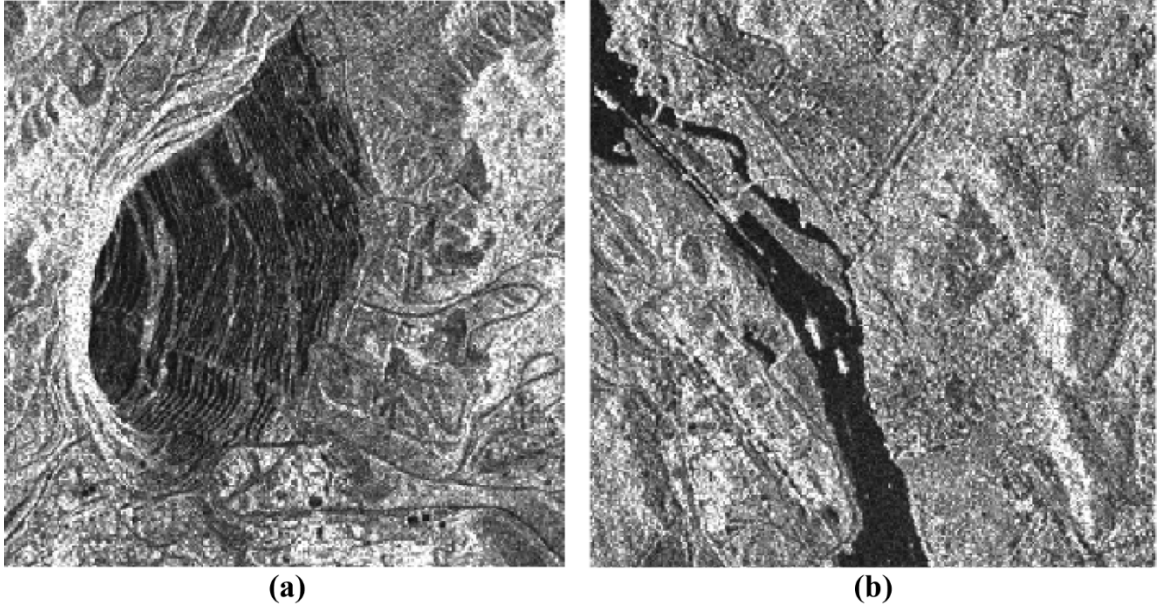
Figure 4.3: Real SAR images. (a) *Chile Copper Mine.* (b) *Panama Canal.*

experiments with a 4-look format and they are shown in Figure 4.3. The Mean and the ENL

values obtained after applying the various despeckling schemes to the two SAR images are

given in Table 4.4. It is noted from this table that the Mean and the ENL values obtained

by applying the proposed scheme are the closest to those one would expect by applying an

ideal despeckling scheme. For a visual comparison of the performances of the various

despeckling schemes, versions of the *Panama Canal* image, despeckled by using these

schemes, are illustrated in Figure 4.4. It is seen from the images of this figure that the S-

Threshold, B-Shrink and Lee-F schemes yield images that lack from an adequate removal

of the speckle noise, and in the case of the S-Threshold scheme, the image also undergoes

an extreme blurriness. On the other hand, the SA-WBMMEA and SARBM3D schemes

over-suppress the speckle noise at the expense of a drastic loss of some of the details of the

SAR image. This loss of details is especially evident from the urban region indicated

Table 4.4: The Mean and the ENL values resulting from applying the various despeckling schemes

| Despeckling scheme | Mean | ENL |
|---|---|---|
| Chile Copper Mine | | |
| S-Threshold | 1.1696 | 2.1721 |
| B-Shrink | **0.9712**[3] | **3.5355**[3] |
| Lee-F | **0.9816**[2] | **3.7379**[2] |
| SAWBMMEA | 0.8924 | 4.5491 |
| SARBM3D | 0.8519 | 4.6379 |
| *Proposed* | **0.9877**[1] | **3.7576**[1] |
| Panama Canal | | |
| S-Threshold | **1.0204**[3] | 2.1655 |
| B-Shrink | 0.9719 | 3.0773 |
| Lee-F | **0.9822**[2] | **3.7818**[2] |
| SAWBMMEA | 0.9075 | **4.3687**[3] |
| SARBM3D | 0.8594 | 4.4239 |
| *Proposed* | **0.9831**[1] | **3.8864**[1] |

[1] First best, [2] Second best, [3] Third best.

by a closed boundary in the images. However, the image despeckled by the proposed scheme exhibits a good speckle suppression accompanied by a superior preservation of the image details.
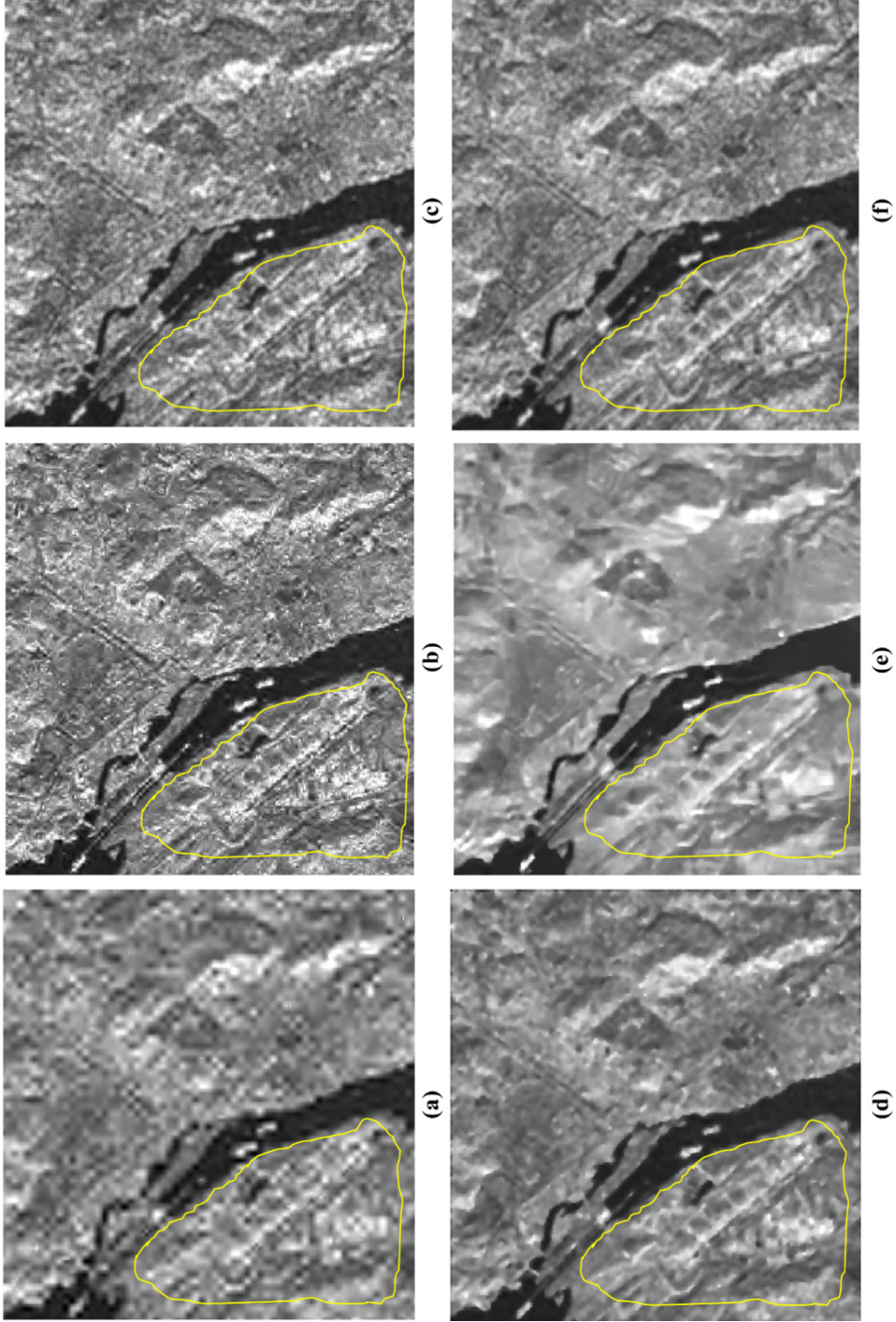
Figure 4.4: The *Panama Canal* image despeckled using the (a) S-Threshold, (b) B-Shrink, (c) Lee-F, (d) SA-WBMMAE, (e) SARBM3D, and (f) Proposed scheme.

## 4.4 Summary

In this chapter, extensive simulations have been carried out to compare the performance of the proposed despeckling scheme with that of several existing techniques using synthetically-speckled and Terrasar-X SAR images. In the case of the synthetically-speckled images, two metrics, namely, SNR and SSIM, have been used to evaluate the performances of the various despeckling schemes in suppressing the speckle noise. To quantify the ability of these schemes in preserving the details original images, the difference in homogeneity, $\Delta\mathcal{H}$, and the difference in correlation, $\Delta\mathcal{C}$, between a noise-free image and a processed image have been used. Computer execution time has been used as a measure of the computational complexity of the schemes. For evaluating the performances of the various schemes in despeckling real SAR images, the Mean and ENL values have been used. In addition to the quantitative evaluations mentioned above, a visual evaluation of the performances of the various despeckling schemes, for both cases of the synthetically-speckled and real SAR images, has also been carried out.

The proposed scheme has been applied first to synthetically-speckled images. The new scheme has been compared with three popular despeckling techniques. The experiments have shown that the proposed scheme provides a performance that is superior to that of these techniques in terms of both the SNR and SSIM values, and has a very competitive or, in some instances, even a lower computational cost. Furthermore, from the values of $\Delta\mathcal{H}$ and $\Delta\mathcal{C}$ obtained in the experiments, it has been seen that the proposed scheme is more effective in preserving the details of the original images. The proposed scheme has been also compared with two powerful state-of-the-art techniques recently

proposed. The experiments have shown that, although the proposed scheme provides SNR and SSIM values that are lower than that provided by these two techniques, it provides better values in terms of homogeneity and correlation differences. In terms of the complexity, the execution time of the proposed scheme is at least an order of magnitude lower than that of these techniques.

The various despeckling schemes have also been applied to real Terrasar-X SAR images. The results have shown that the proposed scheme provides the best Mean and ENL values among all the despeckling techniques considered, thus indicating its ability in providing a good speckle suppression for SAR images along with a superior preservation of the details contained therein.

# CHAPTER 5

# Conclusion

## 5.1 Concluding Remarks

The presence of speckle noise in images affects the tasks of human interpretation and scene analysis, and thus, removal or minimization of such a noise is a vital pre-processing step. Developing effective techniques for image despeckling has been a focus of many researchers in the image processing community. Early-developed techniques have been of a low-complexity at the expense of not achieving a satisfactory despeckling performance. Some recent techniques have proven to be quite effective in suppressing the speckle noise but with some loss of image details in the despeckled images. These techniques, however, often require an enormous computational time. The objective of this study has been to develop an image despeckling scheme of a low-complexity that simultaneously provides a sufficient despeckling performance without over-smoothing the image details.

In order to meet the stated objective, a wavelet-based despeckling scheme has been developed in a framework of Bayesian estimation. The proposed scheme is based on decomposing the multiplicative degradation model of the noisy image as a sum of noise-

free and noise-dependant components. In the first part of this work, a study has been undertaken to investigate the suitability of a distribution to model the wavelet coefficients of the noise-dependent component. It has been demonstrated that the two-sided exponential distribution is capable of accurately modeling the wavelet coefficients of this component of the image. This distribution modeling the wavelet coefficients of the noisy component along with the Cauchy distribution, which is known to be suitable to model the wavelet coefficients of the noise-free component of an image, has been employed to formulate a MMSE Bayesian shrinkage function to obtain the estimates of the noise-free wavelet coefficients. A low-complexity, and yet accurate, realization of this shrinkage function has been proposed.

Experiments have been conducted on both synthetically-speckled and Terrasar-X SAR images in order to demonstrate the performance of the proposed despeckling scheme. It has been shown that the proposed scheme provides not only a significant reduction in the speckle noise at a very low computational cost but also preserves the image details. The proposed scheme provides a substantially-improved despeckling performance over that of some of the popular despeckling techniques proposed earlier at a very competitive computational cost. On the other hand, in contrast to some powerful state-of-the-art techniques, the proposed scheme provides a reduction in the speckle noise without over-smoothing the image to the extent of losing its details and does so at a computational cost that is orders of magnitude lower.

## 5.2  Scope for Further Work

One can further extend the research work undertaken in this thesis. In the Bayesian despeckling scheme developed in this thesis, the estimates of the noise-free DWT

coefficients are obtained without taking into account the dependencies among the DWT coefficients. Providing a spatial adaptation to account for these dependencies may improve the despeckling performance. Hence, an interesting scope for further investigation would be to incorporate the spatial adaptation in the despeckling scheme developed in this thesis. However, an obvious challenge in solving this problem would be to develop the spatially-adaptive scheme without significantly increasing the computational cost.

Another interesting area of investigation would be to explore new statistical models for the DWT coefficients of the signal-dependant noise of the observed signal with a view to achieve a closed-form expression of the MMSE Bayesian shrinkage function. Having a closed-form expression of the Bayesian shrinkage function can further reduce the computation effort of estimating the noise-free DWT coefficients. However, the challenge in proposing a new distribution to model the wavelet coefficients in order to achieve a close-form shrinkage function would be in ensuring the new model to accurately match the empirical distribution of the wavelet coefficients.

# REFERENCES

[1] R. Touzi, "A review of speckle filtering in the context of estimation theory," *IEEE Transactions on Geoscience and Remote Sensing,* vol. 40, no. 11, pp. 2392-2404, Nov. 2002.

[2] J. S. Lee, "Refined filtering of image noise using local statistics," *Computer Graphics and Image Processing,* vol. 15, no. 4, pp. 380-389, Sept. 1981.

[3] V. S. Forst, J. A. Stiles, K. S. Shanmugan, and J. C. Holtzman, "A model of radar images and its application to adaptive digital filtering of multiplicative noise," *IEEE Transactions on Pattern Analysis and Machine Intelligence,* vol. PAMI-4, no. 2, pp. 157-166, Mar. 1982.

[4] A. Lopes, R. Touzi, and E. Nezry, "Adaptive speckle filters and scene heterogeneity," *IEEE Transactions on Geoscience and Remote Sensing,* vol. 28, no. 6, pp. 992-1000, Nov. 1990.

[5] E. Nezry, A. Lopes, and R. Touzi, "Detection of structural and textural features for SAR image filtering," in *Geoscience and Remote Sensing Symposium, 1991. IGARSS '91. Remote Sensing: Global Monitoring for Earth Management., International*, 1991, pp. 2169-2172.

[6] J. S. Lee, J. H. Wen, T. L. Ainsworth, K. S. Chen, and A. J. Chen, "Improved sigma filter for speckle filtering of SAR imagery," *IEEE Transactions on Geoscience and Remote Sensing,* vol. 47, no. 1, pp. 202-213, Jan. 2008.

[7] X. Z. Yang and D. A. Clausi, "Structure-preserving speckle reduction of SAR images using nonlocal means filters," presented at the Image Processing (ICIP), 2009 16th IEEE International Conference on, 2009.

[8] G. T. Li, C. L. Wang, P. P. Huang, and W. D. Yu, "SAR image despeckling using a space-domain filter with alterable window," *IEEE Geoscience and Remote Sensing Letters,* vol. 10, no. 2, pp. 263-267, Mar. 2013.

[9] D. L. Donoho, "Denoising by soft-thresholding," *IEEE Transactions on Information Theory,* vol. 41, no. 3, pp. 613-627, May 1995.

[10]  E. P. Simoncelli and E. H. Adelson, "Noise removal via Bayesian wavelet coring," in *Image Processing, 1996. Proceedings., International Conference on*, Lausanne, 1996, pp. 379-382.

[11]  S. Fukuda and H. Hirosawa, "Suppression of speckle in synthetic aperture radar images using wavelet," *International Journal of Remote Sensing,* vol. 19, no. 3, pp. 507-519, Feb. 1998.

[12]  E. P. Simoncelli, "Bayesian denoising of visual images in the wavelet domain," in *Lecture Notes in Statistics*, P. Muller and B. Vidakovi, Eds., ed New York: Springer-Verlag, 1999, pp. 291–308.

[13]  A. Achim, P. Tsakalides, and A. Bezerianos, "SAR image denoising via Bayesian wavelet shrinkage based on heavy-tailed modeling," *IEEE Transactions on Geoscience and Remote Sensing,* vol. 41, no. 8, pp. 1773-1784, Aug. 2003.

[14]  G. Moser, J. Zerubia, and S. B. Serpico, "SAR amplitude probability density function estimation based on a generalized Gaussian model," *IEEE transactions on image processing,* vol. 15, no. 6, pp. 1429-42, June 2006.

[15]  M. I. H. Bhuiyan, M. O. Ahmad, and M. N. S. Swamy, "Spatially adaptive wavelet-based method using the Cauchy prior for denoising the SAR images," *IEEE Transactions on Circuits and Systems for Video Technology,* vol. 17, no. 4, pp. 500-507, Apr. 2007.

[16]  T. Bianchi, F. Argenti, and L. Alparone, "Segmentation-based MAP despeckling of SAR images in the undecimated wavelet domain," *IEEE Transactions on Geoscience and Remote Sensing,* vol. 46, no. 9, pp. 2728-2742, Sept. 2008.

[17]  A. Achim, A. Bezerianos, and P. Tsakalides, "Novel Bayesian multiscale method for speckle removal in medical ultrasound images," *IEEE Transactions on Medical Imaging,* vol. 20, no. 8, pp. 772-83, Aug. 2001.

[18]  S. Gupta, R. C. Chauhan, and S. C. Sexana, "Wavelet-based statistical approach for speckle reduction in medical ultrasound images," *Med Biol Eng Comput,* vol. 42, no. 2, pp. 189-92, Mar 2004.

[19]  S. Foucher, G. B. Benie, and J. M. Boucher, "Multiscale MAP filtering of SAR images," *IEEE Transactions on Image Processing,* vol. 10, no. 1, pp. 49-60, Jan. 2001.

[20]  F. Argenti and L. Alparone, "Speckle removal from SAR images in the undecimated wavelet domain," *IEEE Transactions on Geoscience and Remote Sensing,* vol. 40, no. 11, pp. 2363-2374, Nov. 2002.

[21] M. Dai, C. Peng, A. K. Chan, and D. Loguinov, "Bayesian wavelet shrinkage with edge detection for SAR image despeckling," *IEEE Transactions on Geoscience and Remote Sensing,* vol. 42, no. 8, pp. 1642-1648, Aug. 2004.

[22] S. Solbo and T. Eltoft, "Homomorphic wavelet-based statistical despeckling of SAR images," *IEEE Transactions on Geoscience and Remote Sensing,* vol. 42, no. 4, pp. 711-721, Apr. 2004.

[23] C. Oliver and S. Quengan, *Understanding Synthetic Aperture Radar Images.* NC, USA: SciTech Publishing inc., 2004.

[24] S. Mallat, "A theory for multiresolution signal decomposition: The wavelet representaion," *IEEE Transactions on Pattern Analysis and Machine Intelligence,* vol. 11, no. 7, pp. 674-693, July 1989.

[25] I. Daubechies, *Ten Lectures on Wavelets.* Pennsylvania: SIAM, 1992.

[26] G. Strang and T. Nguyen, *Waveltes and Filter Banks.* Wellesely, Massachusetts: Wellesley-Cambridge Press, 1996.

[27] J. C. Chan and A. K. Goswami, *Fundamentals of Wavelets, Theory, Algorithms, and Application.* New York: John Wiley & Sons, 1999.

[28] R. C. Gonzalez and R. E. Woods, *Digital Image Processing.* Delhi, India: Pearson Education Asia, 2002.

[29] M. Vetterli, "Filter banks allowing perfect reconstruction," *Signal Processing,* vol. 10, no. 3, pp. 219-244, 1986.

[30] S. Mallat, *A Wavelet Tour of Signal Processing.* San Diego, California: Academic Press, 1998.

[31] D. L. Donoho and I. M. Johnstone, "Ideal spatial adaptation by wavelet shrinkage," *Biometrika,* vol. 81, no. 3, pp. 425-455, Sept. 1994.

[32] D. L. Donoho and I. M. Johnstone, "Minimax estimation via wavelet shrinkage," Stanford1992.

[33] I. Daubechies, "Orthonormal bases of compactly supported wavelets," *Communications on Pure and Applied Mathematics,* vol. 41, no. 7, pp. 909–996 Oct. 1988.

[34] A. Cohen, I. Daubechies, and J. C. Feauveau, "Biorthogonal bases of compactly supported wavelets," *Communications on Pure and Applied Mathematics,* vol. 45, no. 5, pp. 485-560, June 1992.

[35] G. Moser, J. Zerubia, and S. B. Serpico, "Finite mixture models and stochastic expectation-maximization for SAR amplitude probability density function estimation based on a dictionary of parametric families," in *Geoscience and Remote Sensing Symposium, 2004. IGARSS '04. Proceedings. 2004 IEEE International*, 2004, pp. 1510-1513.

[36] G. Moser, J. Zerubia, and S. B. Serpico, "Dictionary-based stochastic expectation-maximization for SAR amplitude probability density function estimation," *IEEE Transactions on Geoscience and Remote Sensing,* vol. 44, no. 1, pp. 188-200, Jan. 2006.

[37] M. Wainwright and E. P. Simonelli, "Scale mixtures of Gaussian and the statistics of natural images," in *Adv. Neural Information Processing Systems*. vol. 12, ed Cambridge, Massachusetts: MIT Press, 2000, pp. 855-861.

[38] J. Portilla, V. Strela, M. J. Wainwright, and E. P. Simoncelli, "Adaptive Wiener denoising using a Gaussian scale mixture model in the wavelet domain," presented at the Image Processing, 2001. Proceedings. 2001 International Conference on Thessaloniki, Greece, 2001.

[39] M. Abramowitz and I. Stegun, *Handbook of Mathematical Functions with Formulas, Graphs and Mathematical Tables*. New York: Dover, 1965.

[40] M. I. H. Bhuiyan, M. O. Ahmad, and M. N. S. Swamy, "Wavelet-based despeckling of medical ultrasound images with the symmetric normal inverse Gaussian prior," presented at the Acoustics, Speech and Signal Processing, 2007. ICASSP 2007. IEEE International Conference on, Hawaii,USA, 2007.

[41] C. Guozhong and L. Xingzhao, "Cauchy pdf modelling and its application to SAR image despeckling," *Journal of Systems Engineering and Electronics* vol. 19, no. 4, pp. 717-721 Aug. 2008.

[42] S. V. Vaseghi, *Advanced Digital Signal Processing and Noise Reduction*: John Wiley & Sons, 2000.

[43] J. M. Nicolas, "Introduction to second kind statistic: application of log-cummulants to SAR image law analysis," *Traitement du Signal,* vol. 12, no. 3, pp. 139-167, Mar. 2002.

[44] I. Gradshteyn and I. Ryzhik, *Table of Integrals, Series, and Products*, 7 ed. San Diego, California: Academic Press, 2007.

[45] H. Vincent Poor, *An Introduction to Signal Detection and Estimation*. New York: Springer-Verlag, 1988.

[46] W. H. Press, S. A. Teukolskym, W. T. Vellering, and B. P. Flannery, *Numerical Recipes in C: The Art of Scientific Computing.* Cambridge, U. K.: Cambridge University Press, 1999.

[47] Wolfram Research Inc., "Mathematica," 8.0 ed. Champaign, Illinois: Wolfram Research, Inc., 2010.

[48] S. G. Chang, B. Yu, and M. Vetterli, "Adaptive wavelet thresholding for image denoising and compression," *IEEE Transactions on Image Processing,* vol. 9, no. 9, pp. 1532-1546, Sept. 2000.

[49] S. Parrilli, M. Poderico, C. V. Angelino, and L. Verdoliva, "A nonlocal SAR image denoising algorithm based on LLMMSE wavelet shrinkage," *IEEE Transactions on Geoscience and Remote Sensing,* vol. 50, no. 2, pp. 606-616, Feb. 2012.

[50] *The MathWorks, Inc., File exchange.* Available: http://www.mathworks.com/matlabcentral/fileexchange

[51] *Università degli Studi di Napoli, Federico II. Image processing research group.* Available: http://www.grip.unina.it/research/80-sar-despeckling/80-sar-bm3d

[52] M. I. H. Bhuiyan, "Spatially-Adaptive Wavelet-Based Techniques for Despeckling of Synthetic Aperture Radar and Medical Ultrasound Images," Ph.D., Electrical and Computer Engineering, Concordia university, Montreal, Quebec.

[53] Z. Wang, A. C. Bovik, H. R. Sheikh, and E. P. Simoncelli, "Image quality assessment: From error visibility to structural similarity," *IEEE Transactions on Image Processing,* vol. 13, no. 4, pp. 600-612, Apr. 2004.

[54] M. Walessa and M. Datcu, "Model-based despeckling and information extraction from SAR images," *IEEE Transactions on Geoscience and Remote Sensing,* vol. 38, no. 9, pp. 2258–2269, Sept. 2000.

[55] H. Breit, T. Fritz, U. Balss, M. Lachaise, A. Niedermeier, and M. Vonavka, "Terrasar-x SAR processing and products," *IEEE Transactions on Geoscience and Remote Sensing,* vol. 48, no. 2, pp. 727–740, Feb. 2010.

[56] *Airbus Defence and Space.* Available: http://www.geoairbusds.com/en/23-sample-imagery